Stellar Metallicities and Kinematics in a Gas-Rich Dwarf Galaxy: First Calcium Triplet Spectroscopy of RGB Stars in WLM

by

Ryan Leaman
B.Sc. University of Washington 2005

A Thesis Submitted in Partial Fullfillment of the
Requirements for the Degree of

MASTER OF SCIENCE

in the Department of Physics and Astronomy, University of Victoria

Stellar Metallicities and Kinematics in a Gas-Rich Dwarf Galaxy: First Calcium Triplet Spectroscopy of RGB Stars in WLM

By

Ryan Leaman

B.Sc. University of Washington 2005

Supervisory Committee

Dr. Kim Venn, Supervisor
Department of Physics and Astronomy, University of Victoria

Dr. Don VandenBerg, Member
Department of Physics and Astronomy, University of Victoria

Dr. Andrew Cole, Member
Department of Mathematics and Physics, University of Tasmania

Supervisory Committee

Dr. Kim Venn, Supervisor
Department of Physics and Astronomy, University of Victoria

Dr. Don VandenBerg, Member
Department of Physics and Astronomy, University of Victoria

Dr. Andrew Cole, Member
Department of Mathematics and Physics, University of Tasmania

Abstract

We present the first determination of the radial velocities and metallicities of 78 red giant stars in the isolated dwarf irregular galaxy WLM. Observations of the calcium II triplet in these stars were made with FORS2 at the VLT-UT2 in two separated fields of view in WLM, and the [Fe/H] values were conformed to the Carretta and Gratton (1997) ($[\mathrm{Fe/H}]_{CG97}$) metallicity scale. The mean metallicity is $\langle[\mathrm{Fe/H}]\rangle = -1.27 \pm 0.04$ dex, with a standard deviation of $\sigma = 0.37$. We find that the stars in the inner field are more metal rich by $\Delta[\mathrm{Fe/H}] = 0.30 \pm 0.06$ dex. These results are in agreement with previous photometric studies that found a radial population gradient, as well as the expectation of higher metallicities in the central star forming regions. Ages are estimated using Victoria-Regina stellar models, and we find that the youngest stars in the sample (< 6 Gyr) are more metal rich by $\Delta[\mathrm{Fe/H}] = 0.32 \pm 0.08$ dex.

These stars also show a lower velocity dispersion at all elliptical radii compared to those of the metal-poor stars. Additionally, the stellar kinematics suggest a velocity gradient approximately half that of the gas rotation curve, with the stellar components occupying a thicker disk decoupled from the H I rotation plane. Taken together, the kinematics, metallicities, and ages in our sample suggest a young metal-rich, and kinematically cold stellar population in the central gas-rich regions of WLM, surrounded by a separate dynamically hot halo of older, metal poor stars.

Table of Contents

List of Figures

List of Tables

Acknowledgments

I would like to acknowledge funding and support from Don VandenBerg and Kim Venn, as well as countless hours of help from the two of them. Additional thanks to Andrew Cole, Mike Irwin, Eline Tolstoy, Evan Skillman, Thomas Szeifert and Alan McConnachie for help and useful discussions on this work.

Dedication

Family, friends, and Mortimer the cat.

Chapter 1

Introduction

1.1 Motivation and Background

Dwarf galaxies play a critical role in our understanding of the assembly of galaxies in LCDM cosmologies. With masses of 10^8 to 10^9 $M_\odot$, these galaxies are thought to be similar to the proto-galactic fragments that merged and collapsed to form large galaxies (e.g., Navarro et al. 1997; Moore et al. 1999; Madau et al. 2001). Analysing the survival of these low mass objects, particularly through reionisation (Ricotti and Gnedin, 2005; Gnedin and Kravtsov, 2006), is crucial to constraining galaxy formation models. For example, what was the minimum halo mass that could retain its baryons through reionisation? Theoretical constraints are also provided by examining the detailed characteristics of the various types of dwarf galaxies (irregulars, spheroidals,

and the new ultra faint dwarfs) and the connections between them. Are dIrr galaxies simply dSph which have undergone recent gas mergers, leaving some (or all) of these galaxies in polar ring configurations (Demers et al., 2006; Brook et al., 2007)? Are transition galaxies, gas-rich dwarf galaxies subject to ram pressure stripping (e.g., Pegasus dwarf galaxy; McConnachie et al. 2007)? Would we expect to see signatures of a thick disk or distinct spheroidal components in dIrr galaxies? How will the dynamics of the stellar populations compare to the gas motion in the low mass, gas rich galaxies? This line of research is best carried out on the nearby Local Group galaxies, thus defining near-field cosmology.

Dwarf irregular (dIrr) galaxies hold a special status in the analysis of the Local Group galaxies because most are relatively isolated. Detailed studies of the nearby dwarf spheroidal galaxies have revealed complex and varied star formation histories that have left behind distinct stellar populations (Tolstoy et al., 2004; Battaglia et al., 2006; Bosler et al., 2007). However, interpretation of the kinematics of the stellar populations and therefore evolution of the nearby dSph galaxies, is complicated by the fact that they exist in the dark matter halos of the MW and M31; therefore their stellar populations have likely been tidally stirred. On the contrary, dwarf irregular galaxies are relatively *isolated* low mass galaxies. Evolved stellar populations in the dIrr may prove to be excellent tracers of the dynamical history of low mass dwarf galaxies at early times, and therefore excellent comparisons for galaxy formation

models.

There have been few studies of the kinematics of the stellar populations in isolated dIrrs and no detailed spectroscopic analysis of their *older* stellar populations, due to their distance.[1] This is significant because various galaxy formation scenarios predict different characteristics for the stellar populations in early dwarf galaxies; e.g., simulations by Mayer et al. (2006) predict disk-like systems that become more spheroidal through tidal interactions and ram pressure stripping, whereas Kaufmann et al. (2007) suggest that dwarf galaxies start out as thick, puffy systems and through gas losses and tidal interactions become more disk like.

In this paper, we present the first spectroscopic analysis of the calcium II triplet (CaT) feature in a sample of RGB stars in the dIrr galaxy WLM. WLM is a typical low-luminosity, high gas fraction late-type dwarf irregular galaxy; a summary of its fundamental parameters is listed in Table 1.1 The nearest neighbour to WLM is the Cetus dSph, which lies 200 kpc away (Whiting et al., 1999). WLM's distance to the Milky Way is ∼970 kpc (Gieren et al., 2008), and its separation from M31 is ∼820 kpc, therefore this is one of the most isolated galaxies in the Local Group. WLM has a heliocentric velocity of -130 km s^{-1} Jackson et al. (2004) and a modest velocity with respect to the Local Group barycentre - just -29 km s^{-1}, implying that it may have

[1]We note that Tolstoy et al. (2001) examined the calcium II triplet feature in 23 RGB stars in the closest dIrr, NGC 6822 ($V_{TRGB} \sim 21$), and found most stars were young and metal-rich, representative of the dominant young population at the brightest magnitudes.

only just recently passed apocentre and is turning around. Additionally, WLM lies out of the Galactic plane, which minimizes foreground contamination and reddening.

High dispersion spectra have been taken for a few bright A and B-type supergiant stars in WLM (Venn et al., 2003; Bresolin et al., 2006; Urbaneja et al., 2008). Detailed analyses of these stars provide the present day metallicities and abundance ratios ([Fe/H]= -0.38 ± 0.2, Venn et al. 2003; [O/H]~ -0.85, Bresolin et al. 2006; [Z]= -0.87 ± 0.06, Urbaneja et al. 2008), but offer little information on the intermediate-age or old populations. The older red giant branch stars in these isolated dIrrs are too faint for high dispersion spectroscopic analyses, even with 8m class telescopes. Studies of H II regions from emission line spectroscopy yield [O/H] = -0.83 (Skillman et al., 1989; Hodge and Miller, 1995; Lee et al., 2005) but provide no information about the chemistry of the gas in the early stages of the galaxy. Interestingly, WLM has revealed minor discrepancies in chemistry between the young stars and H II regions - possibly due to inhomogeneous mixing (Venn et al., 2003; Lee et al., 2005). Neutral gas studies in WLM have been used to map the H I envelope extent and small scale spatial and velocity structures (Huchtmeier et al., 1981; Barnes and de Blok, 2004; Jackson et al., 2004; Kepley et al., 2007).

The old population in WLM was first sampled using HST by Hodge et al. (1999) who derived a metallicity from isochrone fitting of the only globular cluster, WLM-1. Deep HST photometry and wide field INT imaging surveys (Minniti and Zijlstra, 1997;

Rejkuba et al., 2000; McConnachie et al., 2005) also identified young and old stellar populations in the form of an extended blue main sequence, and a horizontal branch on the CMD. These photometric surveys were also used to find the distance and reddening to WLM, and to estimate the range in metallicity on the RGB. Photometric analyses of C and M stars in WLM by Battinelli and Demers (2004) have argued against the presence of an old extended halo in WLM, opposite to the conclusion from Minniti and Zijlstra (1997) based on the interpretation of their CMDs. However differential reddening within WLM may be affecting all of these photometric analyses; the recent Spitzer IRAC survey of AGB stars in WLM (Jackson et al., 2007) has shown the patchy presence of dust throughout WLM.

The use of the empirically calibrated near infrared calcium triplet lines provides a new method for studying the stellar population in WLM. Situated at $\lambda \sim$8498, 8542, 8662 Å, they are optimally located with minimal contamination from other spectral features and near the peak in flux for these evolved red stars. The summed equivalent widths of these lines are well calibrated to allow a representative placement of a star onto a given [Fe/H] scale, and sensitive enough from medium resolution spectra to perform well out to large distances in the local volume. The metallicity index is also well correlated with the iron abundances ([Fe/H][2]) determined by Carretta and Gratton (1997) from high dispersion spectroscopy of Galactic globular clusters. This

[2]The notation [Fe/H] = $\log(\mathrm{Fe/H})_*$ - $\log(\mathrm{Fe/H})_\odot$

scale shows a linear correlation with the CaT W' index, unlike the Zinn & West (Zinn and West, 1984) scale based upon the Q_{39} spectrophotometric index. Previous large scale calibration studies (Rutledge et al., 1997; Cole et al., 2004; Carrera et al., 2007b; Battaglia et al., 2007) confirmed the robustness of the CaT method over a range of ages ($0.25 \leq \mathrm{Gyr} \leq 13$) and over the metallicity range expected for the stars in a gas rich dIrr galaxy ($-2.5 \lesssim [\mathrm{Fe/H}] \lesssim +0.47$). A growing number of CaT studies have been carried out for several Local Group galaxies, including the Magellanic clouds (Pont et al., 2004; Cole et al., 2005; Grocholski et al., 2006; Carrera et al., 2007a) and dSph galaxies (Tolstoy et al., 2004; Battaglia et al., 2006; Koch et al., 2006; Bosler et al., 2007), which further tests the robustness of the CaT method in different environments.

In the following sections, we discuss the observations, the data reduction methods, and spectral analysis adopted in this paper. These sections are particularly important since this work represents a CaT analysis of some of the faintest RGB stars for which velocities *and* metallicities have been determined at moderate S/N. The main challenge has been to minimize the velocity and metallicity errors. The final uncertainties are slightly larger than CaT surveys of closer galaxies, however we have been able to determine a new metallicity distribution function for WLM and characterize the spatial and velocity variations in its stellar populations.

Table 1.1. WLM Properties

Quantity	Value	Reference
(l, b)	(75.85, -73.63)	Gallouet et al. (1975)
E(B-V)	0.082 ± 0.02 (mag.)	Gieren et al. (2008)
	0.035 (mag.)	McConnachie et al. (2005)
Distance	970 ± 20 kpc	Gieren et al. (2008)
Eccentricity	0.59	Ables and Ables (1977)
Position Angle	181 (deg.)	Jackson et al. (2004)
Heliocentric Velocity (v_{hel}^{HI})	-130 km s^{-1}	Jackson et al. (2004)
Rotation Velocity (v_{rot}^{HI})	30 km s^{-1}	Kepley et al. (2007)
M_v	14.1 (mag.)	van den Bergh (1994)
M_{dyn}	$2.16 \times 10^9 M_\odot$	Kepley et al. (2007)
M_{HI}	$(6.3 \pm 0.3) \times 10^7 M_\odot$	Kepley et al. (2007)
$[\mathrm{Fe/H}]_{\mathrm{phot}}^{\mathrm{RGB}}$	-1.45 ± 0.2 dex	Minniti and Zijlstra (1997)

Chapter 2

Observations and Data Reduction

2.1 Observation Basics

The Very Large Telescope (VLT), is an array of four 8m class telescopes located on Cerro Paranal in Chile, and operated by the European Southern Observatory. The telescopes, while similar, are each equipped with distinct instruments, and represent some of the most technologically advanced astronomical facilities in the world. For this dataset, the observations were made using the FOcal Reducer and low dispersion Spectrograph-2, or FORS2 instrument. A versatile instrument, FORS2 offers two imaging modes as well as four spectroscopic modes, which coupled with the recently upgraded CCD, make it one of the more powerful instruments available for studying resolved stellar populations.

2.2 Target Selection

Relatively isolated and bright stars near the tip of the RGB ($V_{mag} \sim 23$) were selected from 150 second V and I band preimaging exposures from FORS2, as shown in Figure 2.1. The data were bias corrected and flatfielded in IRAF and instrumental photometry was obtained using DAOPHOT/ALLFRAME (Stetson, 1994). Stars were selected from those within half a magnitude of the RGB tip (instrumental I band) and colors consistent with RGB membership. This meant that stars were selected to have instrumental colours spanning the apparent width of the RGB but with $0.9 \leq (V - I) \leq 2.0$ to avoid heavy contamination by red supergiants and M stars. The targets were selected to encompass a broad area of the galaxy's high density (gas and stellar) regions, as well as lower density outer areas. The FORS2 preimaging photometry was matched to extant INT WFC V, i band photometry of a 0.25 square degree region centered on WLM (see McConnachie et al. (2005) for further details). A list of INT WFC candidate stars was created based on colour, magnitude, and location, and these were further filtered based on sharpness and ellipse parameters. The INT WFC stellar spatial distribution is shown in Figure 2.2, along with a plot comparing the stellar and H I densities from McConnachie et al. (2005) and Jackson et al. (2004) respectively. As the stars were uniformly selected to be bright and isolated, we acknowledge that a selection effect may appear at areas of low stellar density. However this is unavoidable in resolved stellar spectroscopy at such large distances,

and simply necessitates that care be taken in the interpretation of the results. Figure 2.3 shows the location of the selected target stars in the two WLM fields, illustrating the isolated nature of the stars. Four globular clusters (47Tuc, NGC1851, NGC1904, M15) spanning a range of metallicities, were also chosen for calibration purposes, as described in §3.1.1.

2.3 Data Acquisition and Reduction

The observations for this study of WLM and the four calibrating clusters were taken during several nights at the VLT in late 2003. The MXU (Mask eXchange Unit) mode was used with the FORS2 instrument at the Cassegrain unit of VLT's UT4 (Yepun) telescope, which was before the instrument was relocated to UT1 (Antu) in 2004. The 83 RGB stellar targets ranged in magnitude from $22.1 \leq V_{mag} \leq 24.0$, requiring exposure times on the order of 40 minutes for individual images even with an 8m class telescope. Slit acquisition images were taken for approximately 150 seconds in Bessell I band, to confirm the pointing and slit alignment prior to science exposures. The parameters for the object science exposures are shown in Table 2.1.

Table 2.1. Observational Parameters

Target	Mag. Range	Distance (kpc)	R.A.	Dec.	Exp. Time (minutes)
WLM-N	$22.1 \leq V_{mag} \leq 24.0$	970[a]	00:01:58	-15:21:47	320
WLM-B	$22.2 \leq V_{mag} \leq 23.2$	970[a]	00:01:58	-15:28:30	320
NGC 104	$11 \leq V_{mag} \leq 14$	4.5	00:24:05	-72:04:51	1
NGC 1851	$12 \leq V_{mag} \leq 16$	12.1	05:14:06	-40:02:50	1
NGC 1904	$12 \leq V_{mag} \leq 16$	12.9	05:24:10	-24:31:27	1
NGC 7078	$12 \leq V_{mag} \leq 16$	10.3	21:29:58	+12:10:01	1

Note. — The location and distance data for the four calibrating globular clusters is taken from the Harris (1996) catalogue which can be found online at http://physwww.mcmaster.ca/∼harris/mwgc.dat

[a]From Gieren et al. (2008)

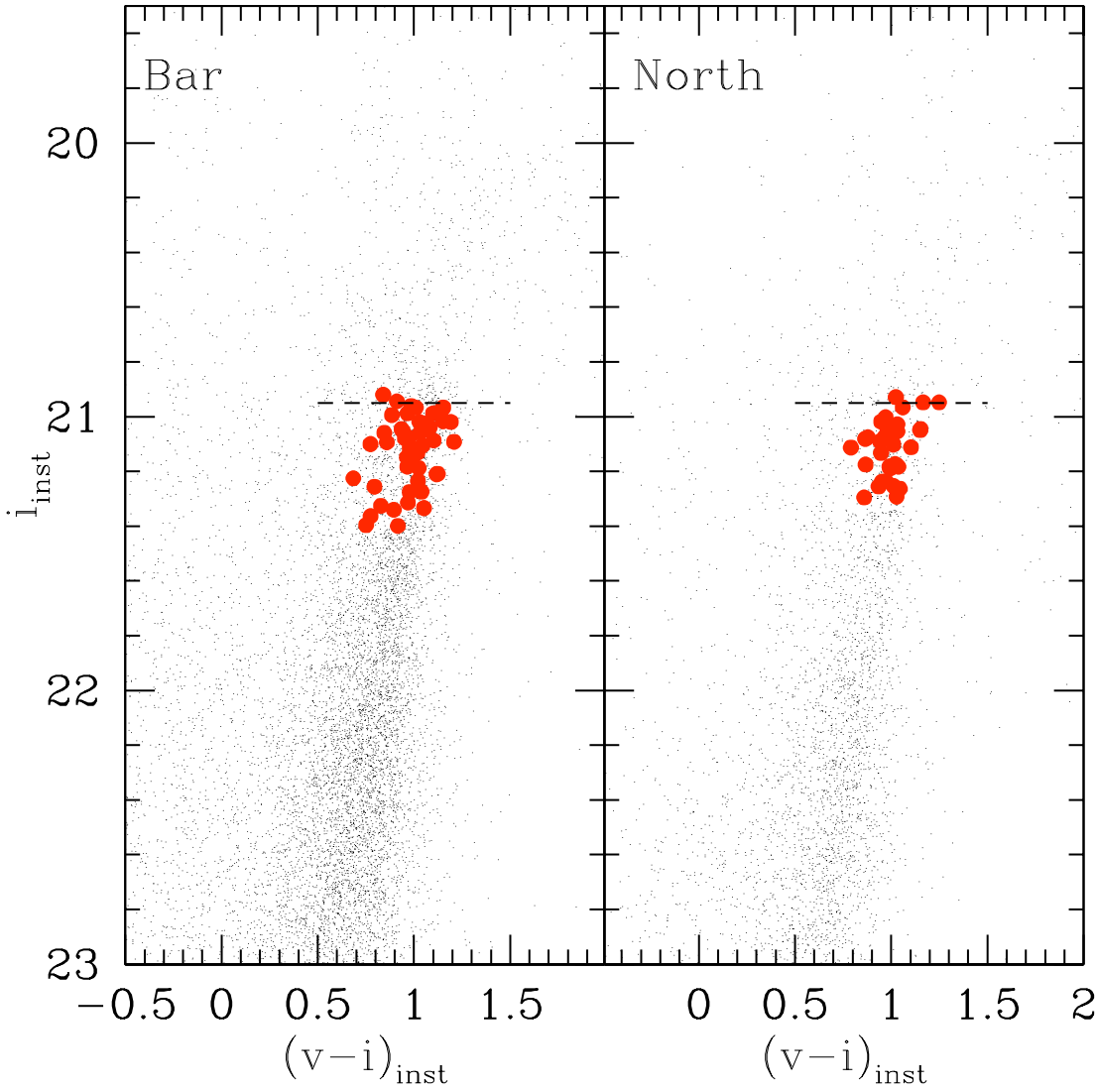

Figure 2.1: Instrumental CMD of WLM, showing the targets near the tip of the RGB for the North and Bar Fields. The instrumental v and i FORS2 magnitudes were later converted to standard systems as described in the text. The preimaging exposures were approximately 150 seconds in each band.

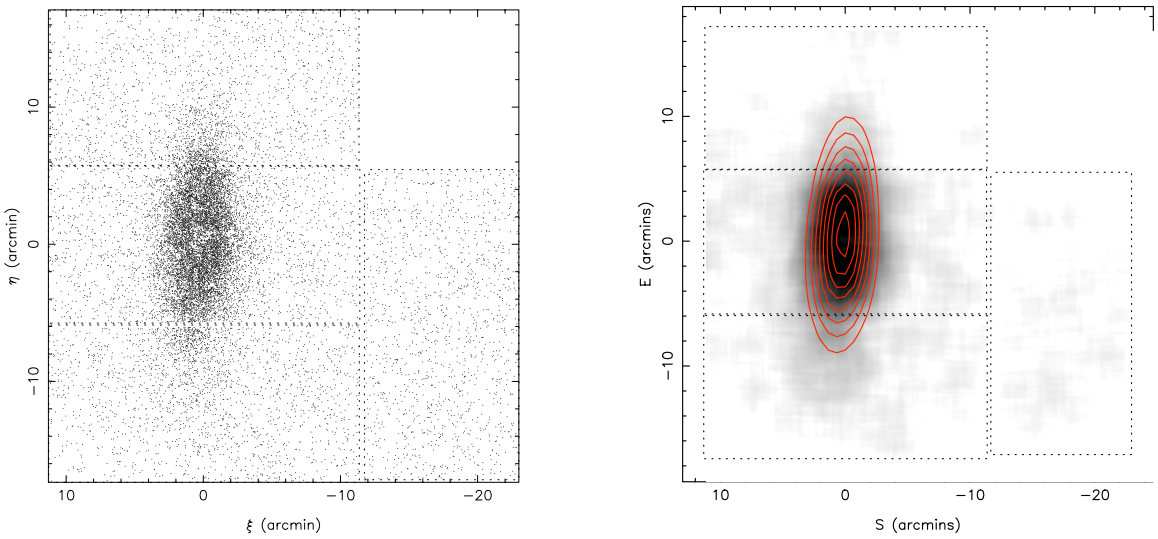

Figure 2.2: (*left panel*) Spatial distribution of stars in the INT WFC photometric catalogue of McConnachie et al. (2005) used in photometric matching. The plot covers a 0.25 degree field of view centered on WLM. (*right panel*) Stellar density (greyscale) of all stars in WLM, with the H I density contours of Jackson et al. (2004) overlaid in red.

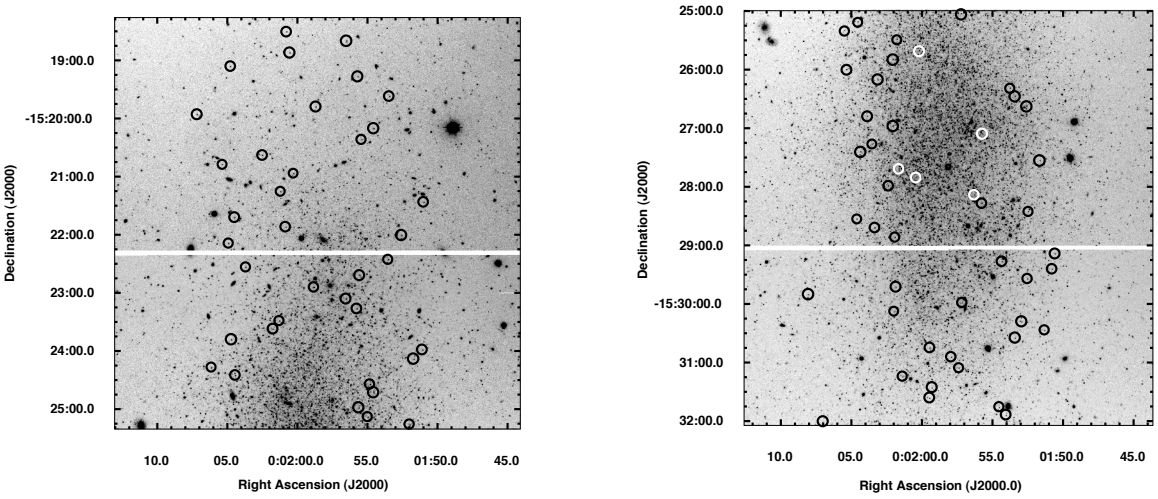

Figure 2.3: FORS2 preimaging for the north (*left panel*), and bar fields in the sample. Shown are the spatial locations of the target stars. Colours of the circles are changed only to aid in visual identification.

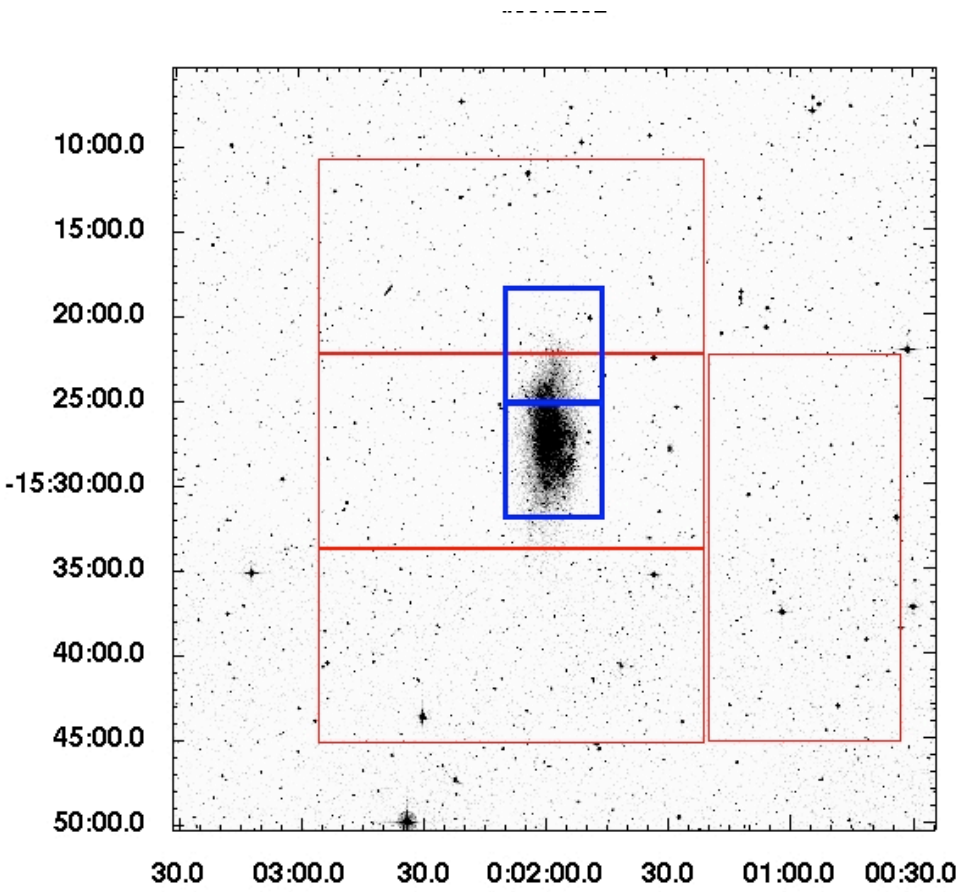

Figure 2.4: Digitized Sky Survey SERC-J image of WLM. The total image is approximately $45' \times 45'$, with North being up and East to the left. The relative locations of the north and bar fields (*blue*) from this FORS2 spectroscopic work are shown. The four red boxes indicate the fields imaged by the INT WFC survey (see McConnachie et al. 2005) The two A-type supergiants from Venn et al. (2003) are located approximately in the centre of the bar field, along with the H II regions from Hodge and Miller (1995), and the B supergiants from Bresolin et al. (2006).

Figure 2.4 shows a representative view of the FORS2/MXU fields used in this study of WLM, with respect to the INT WFC fields of view (the four red rectangles). The FORS2 instrument was used with the MXU in order to provide selectable cus-

tom cut slit plates; a configuration which allowed the preselected RGB stars to be fit within $1'' \times 8''$ slits to minimize the required observation time spent for the program. A spectroscopic order separation filter (OG590+32) and the standard resolution collimator were used in conjunction with a volume phased holographic grism to obtain the stellar spectra for each slit target. The grism, designated GRIS_1028+29, provided wavelength coverage from roughly 7730Å to 9480Å with a central wavelength of $\lambda_c = 8600$Å, and a dispersion of 28.3Å/mm. FORS2 is equipped with a mosaic of two red-optimized 2k×4k MIT CCDs (15μm pixels) with very low fringe amplitude in the spectral range of the CaT lines. With 2×2 binning and 100khz readout characteristics, and the above mentioned optical path, the effective field of view across the instrument was $6.8' \times 5.7'$. The two component chips, from here forth noted as "master" and "slave" have a pixel scale of $0.252''$/pixel (2×2 binning). This setup produced observations with resolving power R $\sim$ 3400. The gain for both chips was 0.7 ADUs/e^-, with the readnoise for the master and slave chips being $2.7e^-$ and $3.15e^-$ respectively. Each of the large blue boxes in Figure 2.4 is representative of the full two chip CCD field of view. The representative seeing conditions for the observations at VLT ranged from $0.61'' \leq$ FWHM $\leq 1.52''$ over the course of the science exposures.

Once obtained in service mode at the telescope, the data were reduced using a

variety of standard IRAF[1] tasks for bias, overscan and flatfield corrections to the two dimensional images. Typically each science image used a bias correction combined from 10 individual bias exposures, along with 5 individual screen flat field exposures for each of the chips (master and slave), which were reduced independently in parallel. The objects were cleaned for cosmic rays using several iterations of the COSMICRAYS task. In order to minimize any error in the final aperture extraction or wavelength calibration, custom tasks were run to remove warping in the stellar trace and sky lines (particularly the far corners of the chips) due to light path distortions or chip alignment issues. A custom IRAF script was used to provide a preliminary correction to the drooping artifact of the stellar trace as a function of row position on the CCD. A second script was then used to linearize and orthogonalize the dispersion coordinate and spatial coordinate to optimize subtraction of the sky lines (see Grocholski et al. 2006). Following these corrections, aperture extraction was run on all science spectra, resulting in one dimensional spectral images for all the stars in the sample. A standard sky line atlas was used in conjunction with the IDENTIFY and REIDENTIFY tasks to provide dispersion solutions for the wavelength calibration of the spectra. Typical line fits involved ~ 40 identified OH sky emission features taken from the Osterbrock and Martel (1992) study. The typical accuracy of the wavelength solution is within

[1]IRAF(Image Reduction and Analysis Facility) is distributed by the National Optical Astronomy Observatory, which is operated by the Association of Universities for Research in Astronomy, Inc., under cooperative agreement with the National Science Foundation

~ 0.04Å based on the rms of the solutions. Finally, the task CONTINUUM removed the curvature of the spectrum and normalized the flux distribution to allow for the most accurate measurements of the regions of interest (the calcium triplet lines).

Prior to combination, the wavelength zeropoint of the stellar spectra was adjusted in order to correct for heliocentric date of observation effects in the spectra. This was a non-trivial concern for the radial velocity measurements as the individual exposures were spread over several months. A date dependent shift was applied to the spectra, as they lacked the signal to noise to be properly combined in rest wavelength space. The spectra were shifted such that their observed velocities were corrected back to a common epoch at the date of the first observation. This resulted in at most a ~ 1.2Å correction to the spectra upon comparison to uncorrected combined images. The final spectra include the median of eight individual exposures for each of 79 RGB stars (four stars were thrown out due to spectral contamination or photometry matching issues). The typical signal to noise ratio for the combined images ranged between $15 \lesssim (\mathrm{S/N}) \lesssim 25$ per pixel (1 pixel = 0.86Å). Figure 2.5 shows a sample spectrum in the region of the Ca II triplet lines for one star in the sample.

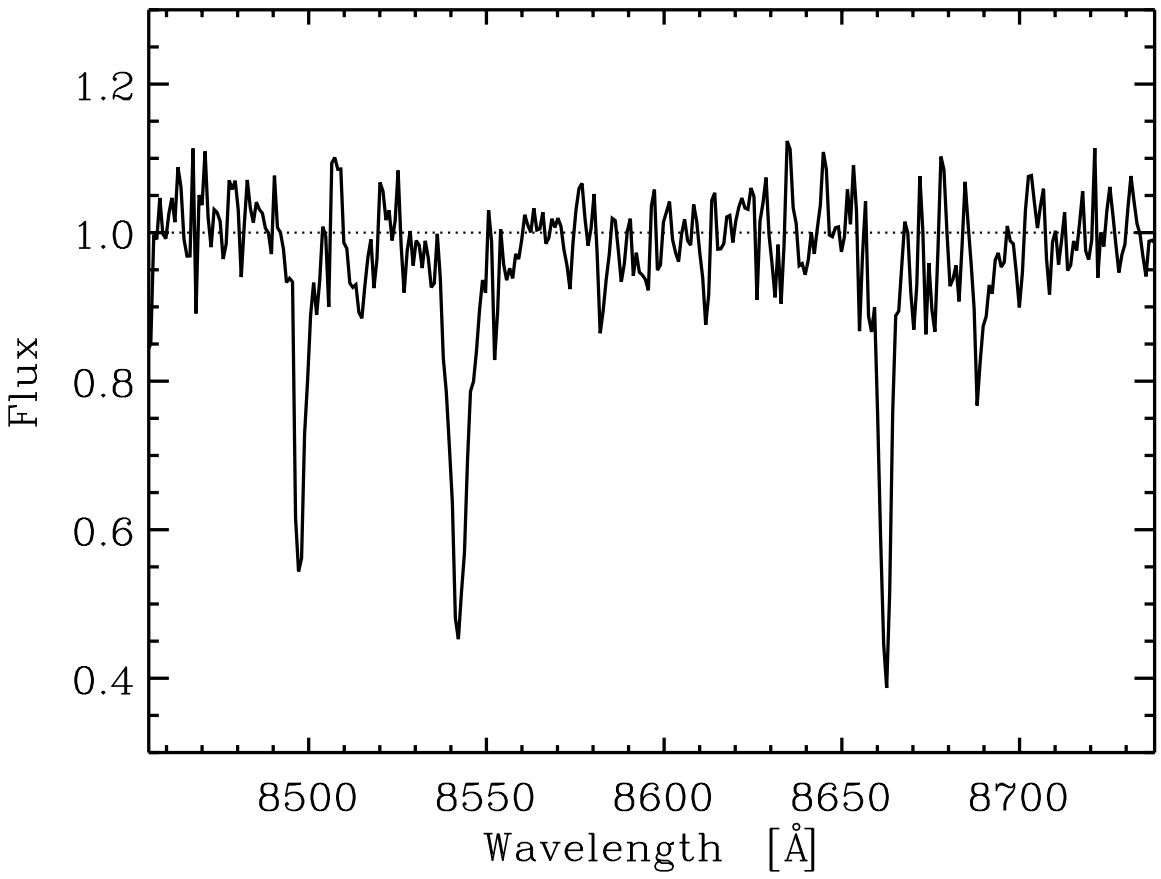

Figure 2.5: Sample combined spectra for one star (STARID 28531) in the WLM FORS2 north field (*top left*). The prominent calcium absorption features are visible at $\lambda\lambda \sim 8498$Å, 8542Å, and 8662 Å even in this (S/N)$\sim$22 image. The y-axis are relative flux units. A dotted line has been drawn at the global continuum level of unity.

Chapter 3

Spectral Analysis

3.1 Equivalent Width Measurements

The choice of techniques for equivalent width measurements had to be carefully considered, given the moderate signal to noise of the combined spectra (~ 20). As noted by Cole et al. (2004), the line wings are typically underestimated with a pure Gaussian profile fit, and are much more accurately modeled with the sum of a Gaussian and Lorentzian fit. However, for low signal to noise spectra when the line FWHM are on the order of the spectral resolution, the contaminating noise features effectively nullify any difference between using a Gaussian, Lorentzian or the sum of the two. Therefore an accurate characterization of the spectrographic setup is necessary in low resolution Calcium triplet spectroscopic studies. This is visualized in Figure 3.1,

which shows the three methods applied to one of the Calcium features in this sample.

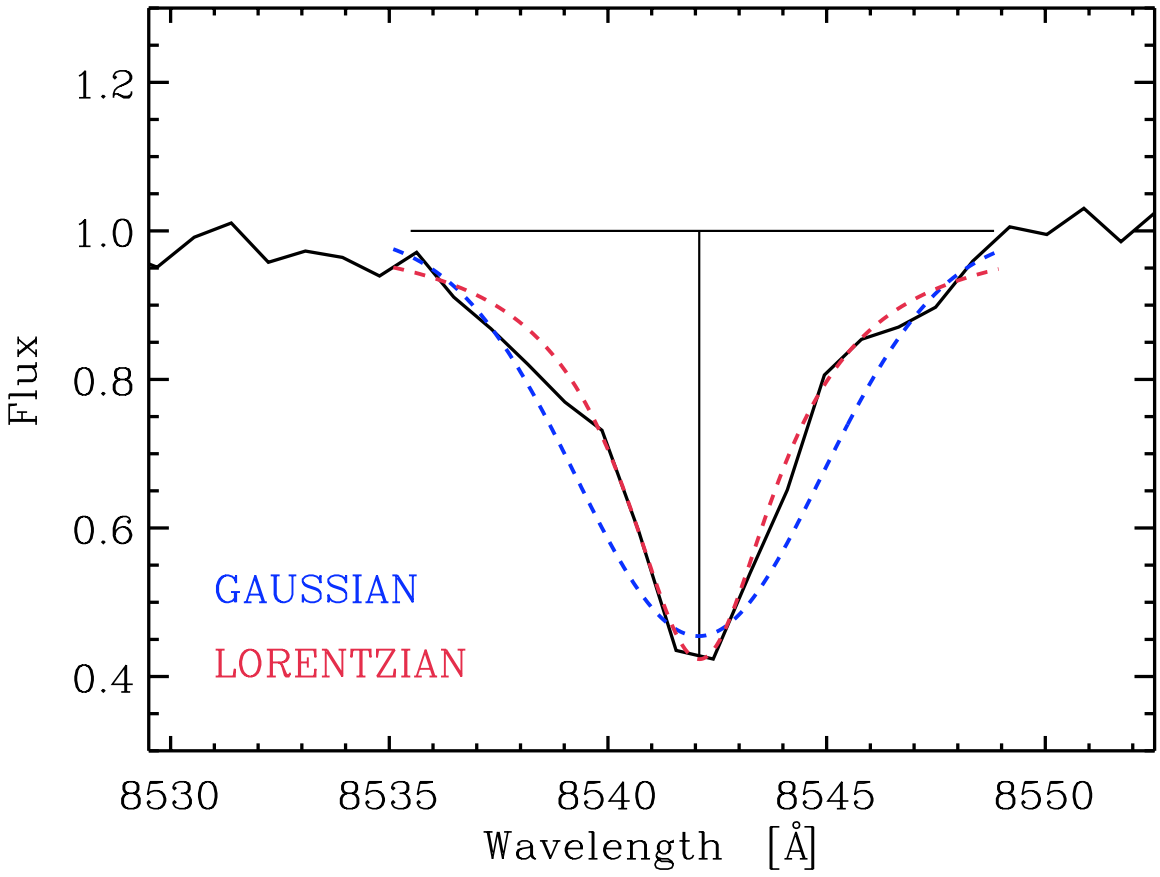

Figure 3.1: Gaussian, Lorenztian fits overlaid onto the Ca II 8542 Å feature. The horizontal line shows the extant of the pixel to pixel integration region below the continuum level (unity). As noted, the two fitted functions differ in their treatments of the line wings, however the spectral resolution and S/N level nullify any difference.

For this reason, the choice was made to use a simple pixel to pixel integration of the line profiles. Due to the low signal to noise of the spectra, the integration was taken over the range where the line wings intersected the global continuum level. The continuum normalized spectra had an average continuum at unity already, no

adjustment was made to the flux zeropoint. The integration yields a wavelength, core density, and equivalent width for each line. Multiple independent measurements were made, by remeasuring the same line repeatedly, with a systematic deviation in equivalent width of approximately 1%.

As a consistency check, simultaneous measurements were made of the reduced calibrating clusters (which had a much higher signal to noise) using both the pixel to pixel integration method and the profile fitting programs from Cole et al. (2004). The linear fit between the methods measurements (see Figure 3.2) was used to develop a transformation function which put our equivalent widths onto the same scale as in Cole et al. (2004), thereby allowing us to adopt a variety of their calibrations as described in the next section.

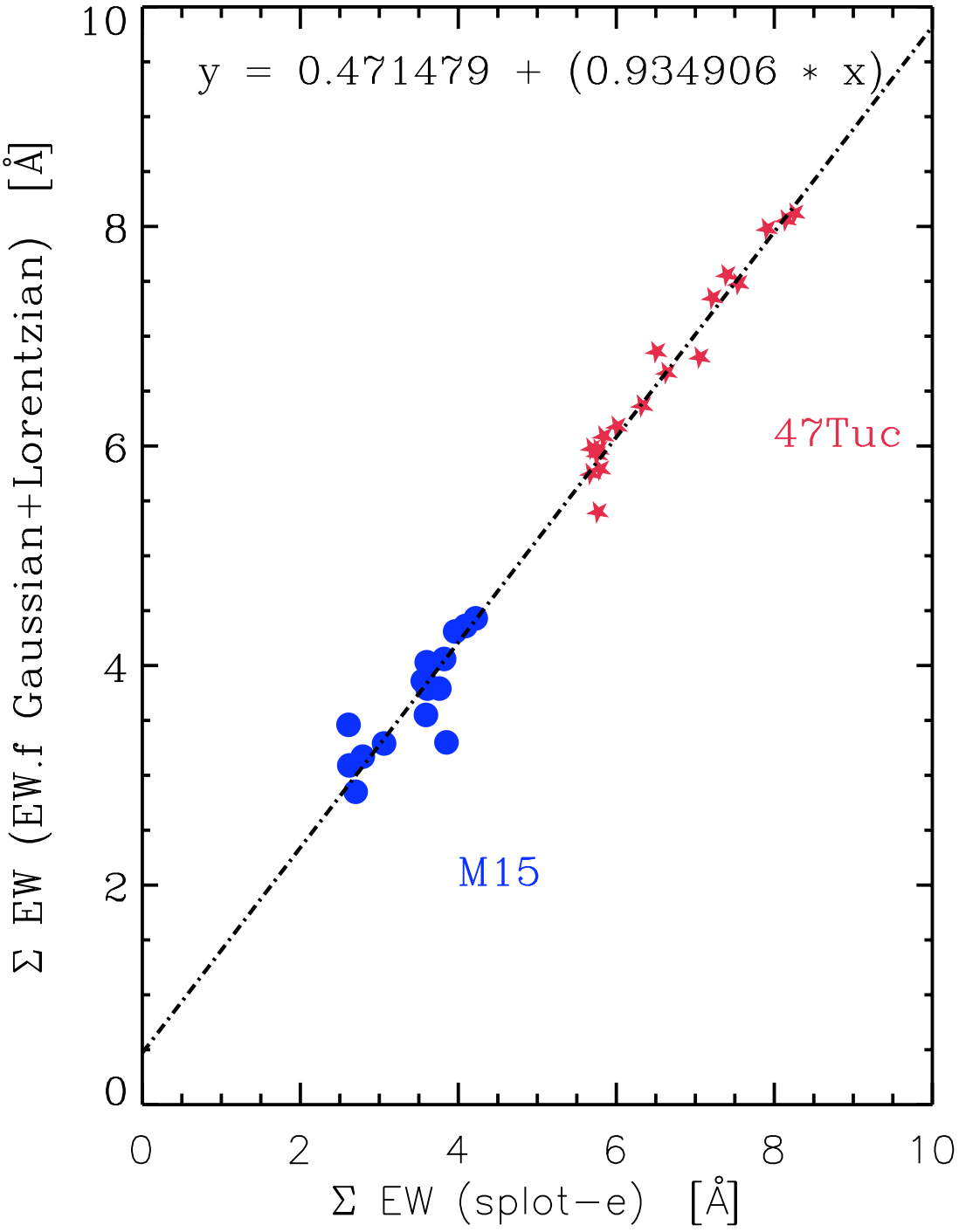

Figure 3.2: Comparison of ΣW measurements using the pixel integration method described in this work, and the Gaussian + Lorentzian profile fits from Cole et al. (2004), for two extreme metal poor and rich calibrating galactic globular clusters. The results of a global linear least squares fit to the two cluster stars is shown as the dot dashed line. The rms dispersion about the fit is 0.22 Å.

3.1.1 *Placement onto the Metallicity Scale*

Armandroff and Da Costa (1991) first showed the usefulness of the CaT feature as a metallicity indicator in individual evolved giant branch stars. Using the summed equivalent widths of the CaT lines, as well as the star's V magnitude above the horizontal branch, a reduced equivalent width could be formulated. When observed for Galactic Globular Cluster stars which also had high dispersion spectroscopic [Fe/H] estimates, this low resolution CaT estimator could be used to provide an empirical metallicity index. Several studies (Rutledge et al., 1997; Cole et al., 2004) have since explored these empirical calibrations over a large range of stellar ages and metallicities. Cole et al. (2004) found minimal deterioration in the CaT calibration over extremes in age and metallicity. This is particularly relevant for dwarf galaxy studies where a mixed stellar population is expected based on CMD analyses (e.g., Dolphin 2000). In this paper, we adopt the calibrations determined by Cole et al. (2004) based on many clusters which were made with the same instrument (FORS2) at the VLT, and adopted similar data reduction techniques as used here. The spread in cluster ages in the full sample studied by Cole et al. (2004) is ideal for analyzing a dIrr galaxy like WLM. Recently, Battaglia et al. (2007) and Carrera et al. (2007b) have confirmed the robustness of the CaT spectroscopic method as a means for metallicity estimates in dwarf galaxies over a large range in parameter space. These studies specifically checked the appropriateness of the CaT index as a proxy for [Fe/H] in cases of varying

[α/Fe], [Ca/Fe], and age. Additionally, studies by Rutledge et al. (1997) and Cenarro et al. (2001) showed that the CaT index transforms in a well understood way between different authors' studies.

To use any of the calibrations requires a summed equivalent width determination for each star. Each of the three calcium triplet line measurements were combined in an unweighted fashion to yield a summed equivalent width per star.

$$\Sigma W = W_{8498} + W_{8542} + W_{8662} \tag{3.1}$$

The justification to use all three lines will be discussed in §3.1.2 and §3.1.3 with respect to our errors. With this relation it is now possible to form the calcium index, W' defined as:

$$W' = \Sigma W + \beta(V - V_{HB}) \tag{3.2}$$

The term in the parentheses provides a correction for the changes in T_{eff} and $log(g)$ for stars in different phases on the red giant branch. A cooler temperature and lower surface gravity play non-trivial roles in the formation of the CaT line profiles and the

continuum in these evolutionary stages. Theoretical and empirical work (Jorgensen et al., 1992; Cenarro et al., 2002) has confirmed this complicated interplay of the calcium line strengths with stellar parameters such as temperature and gravity. This term is important then, in removing the gravity dependence of the lines with respect to the continuum in the CaT analysis. Our V magnitudes are taken from the INT WFC catalogue and associated database as mentioned in §2.2. We adopted the horizontal branch at $V_{HB} = 25.71 \pm 0.09$ mag (Rejkuba et al., 2000), and take $\beta = 0.73 \pm 0.04$Å mag^{-1} from Cole et al. (2004). Using the Carretta and Gratton (1997) scale, the calcium index is converted to a metallicity ([Fe/H]$_{CG97}$) as follows:

$$[Fe/H]_{CG97} = (0.362 \pm 0.014)W' - (2.966 \pm 0.032) \tag{3.3}$$

The zero point and slope were determined by Cole et al. (2004), and estimated as accurate to $\leq 4\%$. This means that the majority of our uncertainties are from other factors, which will be discussed below in the following section.

Figure 3.3 shows a plot of the summed calcium II equivalent widths (ΣW) against the V magnitude above the horizontal branch per star. The fiducial solid lines show the spacing in metallicity given by the calibration from Cole et al. (2004). Figure

3.4 more clearly visualizes the end product of the equivalent width measurements - a metallicity distribution function for all member stars in the sample.

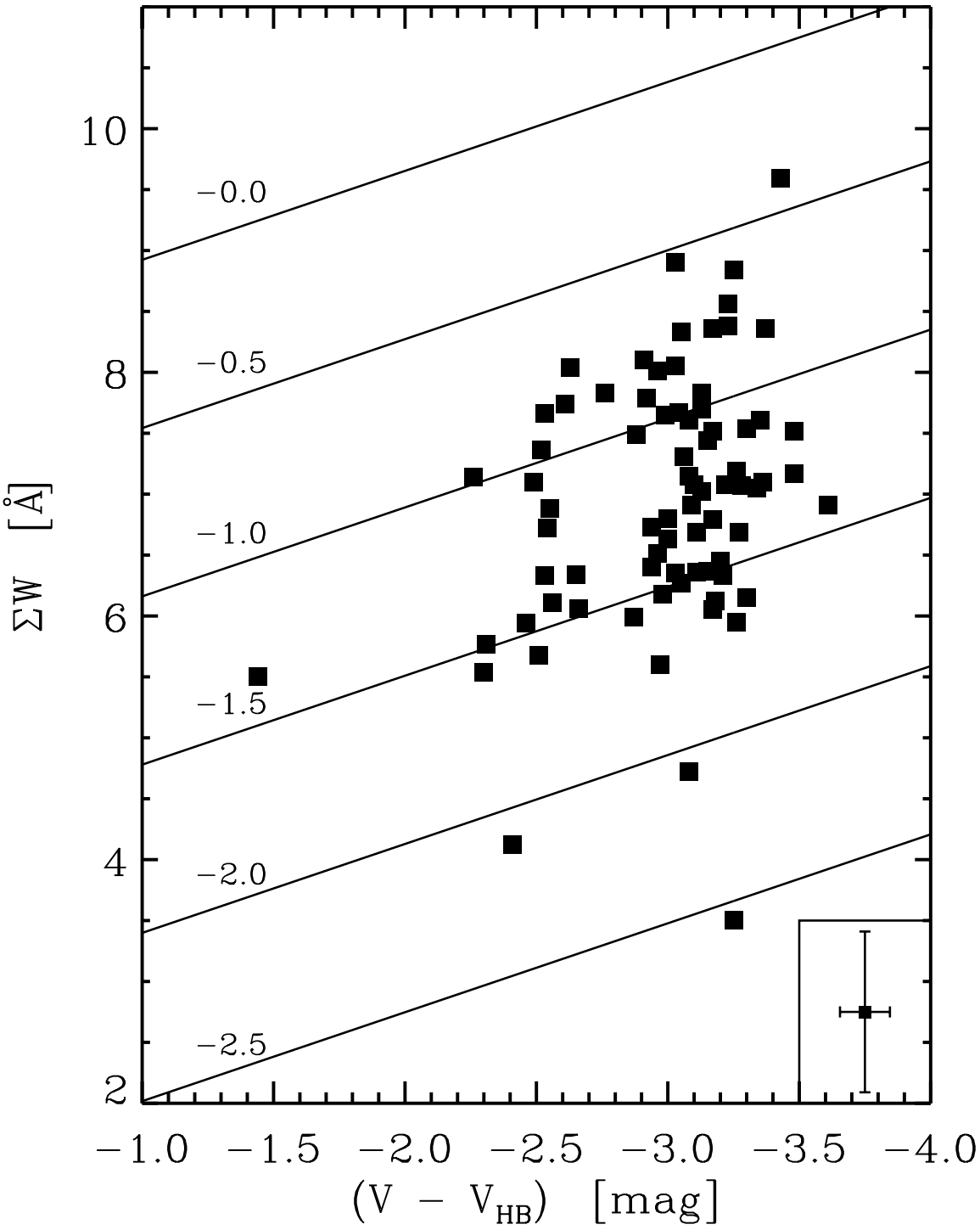

Figure 3.3: Summed equivalent width of the Calcium II triplet lines (ΣW) versus the V magnitude above the horizontal branch. The solid lines show constant metallicity according to the calibration by Cole et al. (2004) which was used to derive our final [Fe/H] values (see text).

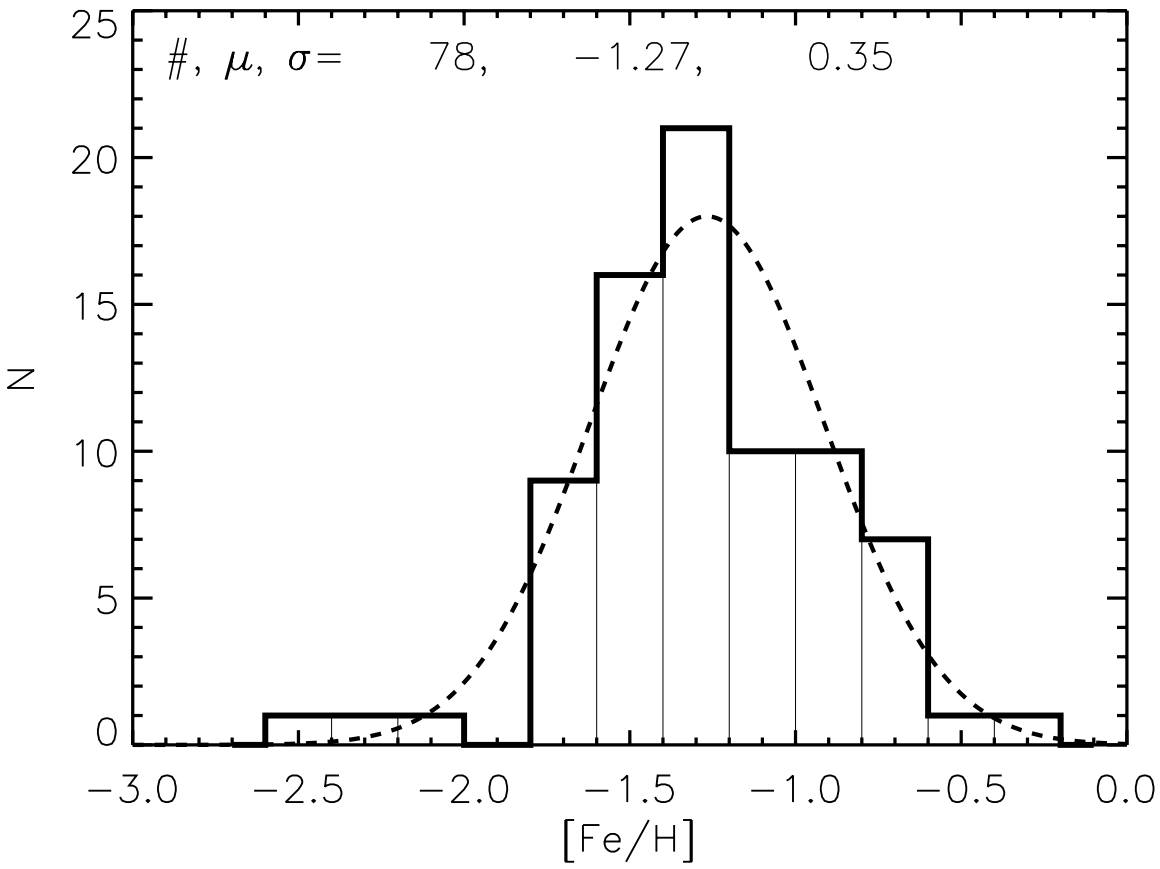

Figure 3.4: Full metallicity distribution for all 78 RGB stars in both FORS2 target fields of WLM. The narrowness and sharp cutoff at both the metal rich tail ($\geq$ -0.5) and metal poor tail ($\leq$ -1.8) is even more clearly seen in this representation. A Gaussian fit is shown by the dashed black line. The median value of the distribution is [Fe/H] = -1.27, and the mean and standard deviation of the Gaussian fit are shown in the figure.

3.1.2 *Error Analysis*

To examine the various sources of uncertainty in our calculations, we kept track of all errors from the equivalent width measurements to placement on the $[Fe/H]_{CG97}$ scale. As no standalone error estimate was provided by the pixel integration routine

used in measuring a line equivalent width, W, we adopted the Cayrel formula (see Cayrel 1988, their Eq. 7; also Battaglia et al. 2007) as:

$$\langle \Delta W_n^2 \rangle^{\frac{1}{2}} \simeq (1.6(FWHM_n \delta x)^{\frac{1}{2}} \epsilon) + (0.10 W_n) \tag{3.4}$$

Where the pixel size is $\delta x = 0.86$Å, and the average rms continuum accuracy is $\epsilon \sim \frac{1}{(S/N)_{avg}}$. As the pixel integration measurements did not contain information on the FWHM of the line, that value was determined as follows. A test set of Gaussian and Lorentzian fits were made to the strongest line (8542 Å)in 18 stars, using the built in line profile fitting routine SPLOT. A Gaussian-Lorentzian blended estimate of the FWHM for this calibration test set was estimated from an arithmetic average of the two fit values. These were then plotted as a function of measured equivalent width (from the pixel integration method). A linear regression was fit and an estimate of the FWHM to be used in this formula for the rest of the stars was done based on their equivalent width values. The FWHM values for the sub-sample of stars used in this step showed a standard deviation of $\sigma_{fwhm} = 1.06$Å.

With a full set of equivalent widths and representative FWHM values, Equation 3.4 could be used to find a realistic uncertainty in a given line. These steps were repeated for all three CaT lines, then added in quadrature for the error in the summed

equivalent width, ΣW. An additional term was added to this in quadrature, to account for the variation in equivalent width measuring methods used. This term was determined from the rms dispersion about the best fit in the transformation to the Cole et al. (2004) EW measurement system (see §3.1.1)

The final expression for the uncertainty in metallicity is now formulated into one equation, allowing for simple partial derivative based error propagation. Defining an equation for metallicity based on the following equation of observables or calibrated variables:

$$f = [Fe/H]_{CG97} = c_1 \left[\Sigma W + \beta(V_{HB} - V)\right] - c_2 \tag{3.5}$$

allowed us to express the total uncertainty as:

$$\Delta[Fe/H]^2 = \left\{ \left(\frac{\partial f}{\partial c_1}\right)^2 (\Delta c_1)^2 + \left(\frac{\partial f}{\partial \Sigma W}\right)^2 (\Delta \Sigma W)^2 + \left(\frac{\partial f}{\partial \beta}\right)^2 (\Delta \beta)^2 + \ldots \right\} \tag{3.6}$$

The simple mathematical propagation is reasonable and justified, as the variables involved in Equation 3.6 are uncorrelated and independent. This propagation and error accounting results in an average uncertainty in metallicity of Δ[Fe/H] = $\pm$0.25

dex.

3.1.3 *Three Line Justification*

A parallel reduction was performed omitting the weakest line in the calcium series (8498 Å). The purpose of this exercise was to test whether the uncertainties in constructing the calcium index, W', were sizeably reduced with the rejection of the lowest signal source. Composite two-line indices were created in order to compare the relative errors that occurred for exclusion of each line in the creation of the calcium index. The *average* relative error for the full 80 star sample on any of the line pairs, $\frac{\Delta W_{nm}}{W_{nm}}$ where n and m are the first, second or third lines of the Ca II triplet, were calculated to be $\frac{\Delta W_{23}}{W_{23}} = 0.10$, $\frac{\Delta W_{13}}{W_{13}} = 0.12$, and $\frac{\Delta W_{12}}{W_{12}} = 0.11$ for the pairs. This minimal deviation, suggests that inclusion of all three lines is warranted, because the EW measures do not dominate the random error budget, and thus there is no benefit to dropping the 8498 Å line.

3.2 Radial Velocity Measurements

Radial velocities were measured from the strong calcium lines which had previously had a wavelength dispersion solution applied from the sky OH lines. The low signal to noise of the individual frames necessitated that the cross correlation radial veloc-

ity calculations were performed on the combined spectra, rather than each individual image. As such, heliocentric velocity corrections were tailored to the individual exposures and applied prior to combining the spectra, due to the long temporal baseline (roughly four months) of the observations. Once shifted and combined, the spectra were ready for radial velocity computation with the aid of template stars and a Fourier cross correlation routine (FXCOR). A total of 23 template radial velocity stars, observed with the same instrument setup, were used with the cross correlation routine. This computation provided error analysis automatically, with the median error in the heliocentric velocities being $\langle \delta V_{hel} \rangle = \pm 6$ km s^{-1}. Systematic velocity errors due to a star's position in the slit were removed by centroiding the stars relative to the slit centre. The fact that this procedure was done on combined spectra resulted in small absolute corrections as the $\sqrt{n}$ statistics meant that the individual slit errors were minimized in the combination and correction steps. The final average absolute corrections to the slit centering errors were on the order of ≤ 1.5 km s^{-1}.

This sample of RGB stars has a mean velocity of $\langle V_{hel} \rangle = -130 \pm 1$ km s^{-1}, identical to the heliocentric velocity for WLM derived from neutral H I studies Jackson et al. (2004); Kepley et al. (2007). Only one foreground star was found, with radial velocity $V_{hel} = +48$ km s^{-1}, leaving us with 78 stars total. Given the location of WLM with respect to the Galactic plane and the colour and magnitude cuts in the preselection routine, it is not surprising that there were so few foreground objects.

Figure 3.5 shows the velocity distribution function for the full sample of member stars in WLM

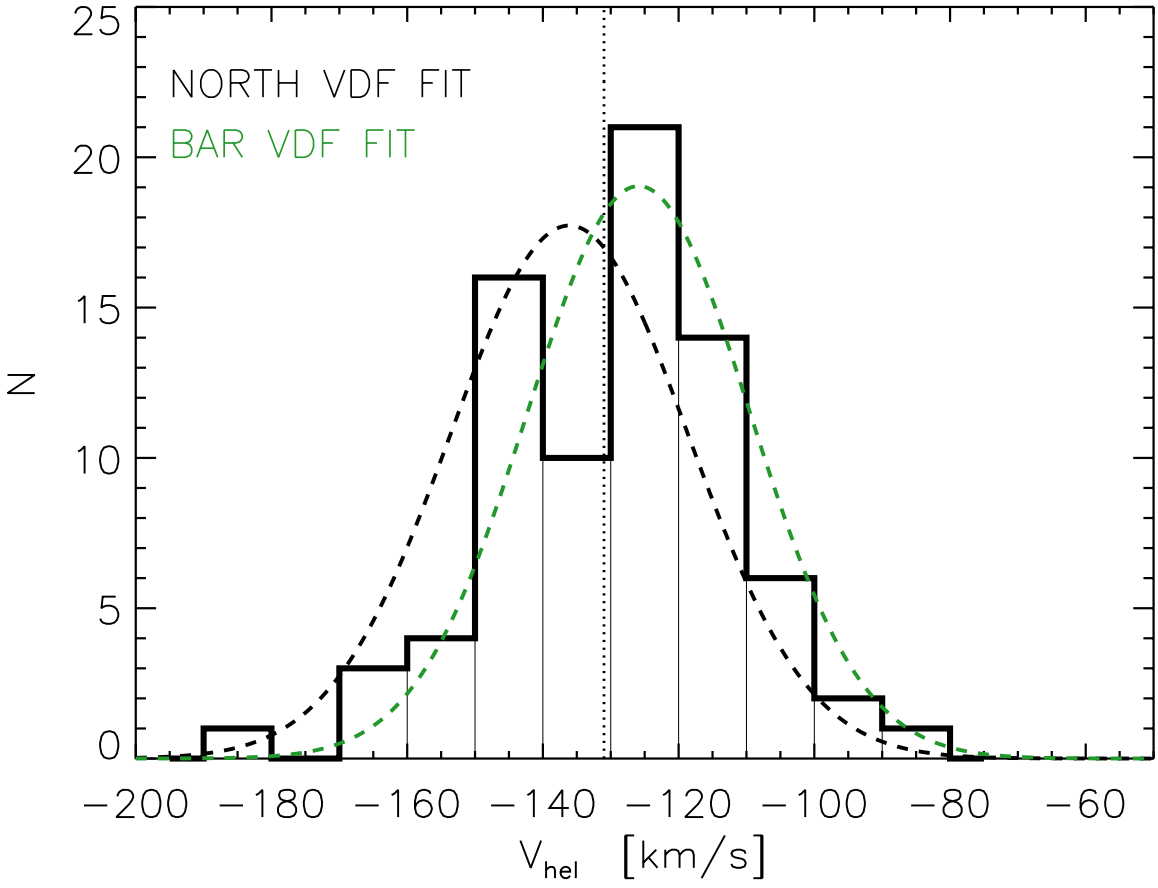

Figure 3.5: Histogram of the heliocentric radial velocity values for all member stars in this sample. Shown are the Gaussian fits to the bar and north field subgroups overlaid on the full distribution, to help illustrate the velocity offset. The systemic velocity of WLM is marked as the dotted vertical line.

3.3 Age Derivations

An estimate of the relative ages of our sample of RGB stars was determined using the Victoria-Regina stellar evolution tracks (VandenBerg et al., 2006). These have a good range and resolution in age (38 values from 0.1 Gyr $\leq t \leq$ 18 Gyr), metallicity (17 values covering $-2.31 \leq$ [Fe/H] ≤ -0.30), and alpha element ratios ([α/Fe]=0.0, 0.3, 0.6) for the anticipated properties of the stars in WLM, and incorporate a recent treatment for convective core overshooting. Given the extended SFH of WLM (Mateo, 1998; Dolphin, 2000) and the gas rich nature of dIrr galaxies, a significant range in red giant ages is expected in the dataset.

This is confirmed qualitatively in Figure 3.6, where the metal poor and metal rich GGC fiducial sequences (M68; [Fe/H]$\sim$-2.0, and 47 Tuc [Fe/H]$\sim$-0.7) are overlaid onto a metallicity binned colour magnitude diagram of WLM. An age spread is clear, as few of the stars have metallicities *more* metal poor than M68 (even within 1.5σ of the [Fe/H] values), yet there are both metal poor and metal rich stars[1] blueward of the fiducial sequence for M68. We also point out one star (STARID 19203), at (V-I)$_0$ $\sim$ 2.2, and note that a greater uncertainty should be applied to this star's parameters as it may be subject to excessive reddening, or spectral contamination (notably, from weak TiO bands). As the stars were selected across a wide range

[1]In this, and other representations throughout the paper, the metallicity split to characterize "metal rich" and "metal poor" RGB stars is made at [Fe/H] = -1.27 dex - approximately the median and mean value of the sample.

in (V-I) colours, the spectroscopic CaT [Fe/H] estimates allow us to break the age-metallicity degeneracy and provide a more complete understanding of the evolved populations in WLM.

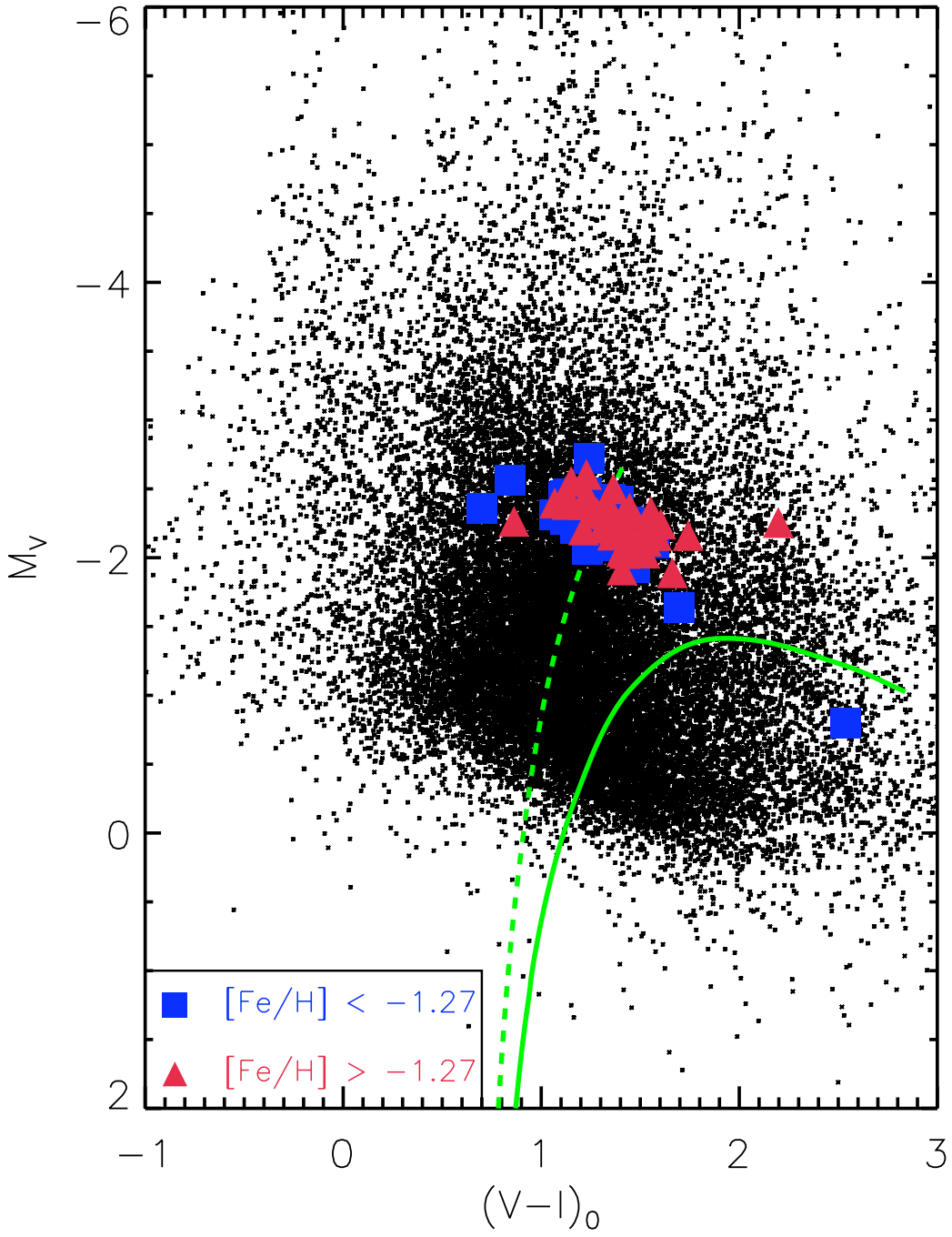

Figure 3.6: CMD of target stars with [Fe/H] ≤ -1.27 (*blue boxes*) and $\geq$ -1.27 (*red triangles*) with the fiducial sequences for 47 Tuc ([Fe/H] $\sim$ -0.7) and M68 ([Fe/H]$\sim$ -2.0; *dashed green line*). The full catalogue of INT WFC photometry is shown as the black dots. It can be seen that there are both metal poor and metal rich stars blueward of the fiducial sequence for M68. This indicates that a younger population is most likely being sampled in some areas. More information on age trends can be found in §4.3.

To determine an age from the Victoria-Regina models, a value of $[Fe/H]_{CaT}$, V, and (V-I) is required for each star, as well as global values for distance and reddening to WLM, and an assumption about the α-element enhancement level. We refrained from binning the stars in our sample by metallicity, instead opting to perform the age interpolation for each individual member so as not to reintroduce any degeneracy from the star's [Fe/H] value. Systematic effects (e.g., an evolutionary model's treatment of mixing length, convective overshooting, CNO abundances, radiative diffusion, gravitational settling etc.) between the models and observations were removed by comparing the isochrones to homogeneous globular cluster photometry from the CADC website[2] of seven galactic globular clusters (47 Tuc, NGC 1851, NGC 288, NGC 7089, NGC 6809, NGC 2298, and M68) over a wide range of metallicities. [Fe/H] values on the Carretta and Gratton (1997) scale were adopted for the clusters based on the compilation in Rutledge et al. (1997), and [α/Fe] taken from Pritzl et al. (2005). A reddening and distance modulus were assigned to the GC fiducials based on the data from the Harris Catalog (Harris, 1996), and each were given an age of 12 Gyr (De Angeli et al., 2005), before bringing them to the dereddened plain with the 12 Gyr Victoria-Regina isochrone of the appropriate metallicity. From there we found the difference in colour that it took to align the full fiducial sequence of each cluster with the single test isochrone in the same plane. The calibration set was in-

[2]url: http://www3.cadc-ccda.hia-iha.nrc-cnrc.gc.ca/community/STETSON/standards/

Table 3.1. Age Interpolation Parameters

Parameter	Value	Reference / Notes
$(m\text{-}M)_0$	24.85 mag	McConnachie et al. (2005)
E(B-V)	0.035 mag	McConnachie et al. (2005)
E(V-I)$\simeq$ E(B-V)$\times$1.242	0.044 mag	Reference from Dean et al. (1978)
$[\alpha/Fe]$	+0.3	See §3.3.1 for discussion
$\delta(V\text{-}I)_{zeropoint}$	0.016 mag	See §3.3.1 for discussion
$\sigma_{(V-I)}$	0.04 mag	Photometric uncertainty

terpolated to provide zeropoint offsets for the complete set of isochrones in the full metallicity space. The offsets were small (the average was Δ(V-I) = 0.016 mag; they ranged from Δ(V-I) = 0.05 at [Fe/H]$\simeq -1.0$, to Δ(V-I) = -0.007 at [Fe/H]$\simeq -2.00$), however they provide reassurance that the evolutionary models are well calibrated. With the theoretical and observational dataset brought to the same plane it was possible to proceed. Table 3.1 shows the assumed global properties adopted for the age determinations. Without a priori knowledge on the [α/Fe] ratio, it was adopted as +0.3 based on evidence from galactic globular clusters, and other Local Group dwarf galaxies (Tolstoy et al., 2003) - however the result of varying this will be discussed later in the paper.

The location of each star in the dereddened plane was then used to interpolate a best age estimate amoung tracks of the appropriate metallicity for that star as follows. For a given star, the set of isochrones with a metallicity most closely matching

the target stars [Fe/H] value from the CaT spectroscopy was selected. Typically the increment in [Fe/H] between tracks was ∼0.1 dex; less than the uncertainty of our spectroscopically derived values of [Fe/H]. This meant that the metallicity value assigned to the model space ($[Fe/H]_{isochrone}$) introduced a negligible uncertainty. Tracks of all the ages at the appropriate metallicity were then laid down in the M_V, $(V\text{-}I)_0$ plane, along with the position of the WLM star in this dereddened, common distance plane. An iterative minimization found the best isochrone age that was radially closest to the star location.

RGB stars can only evolve to luminosities approaching the tip of the RGB when the core becomes significantly electron-degenerate before the onset of core helium burning. Thus there is a lower limit to the age of the first-ascent RGB stars that could possibly be included in our sample, typically around 1.6 Gyr (if significant core overshooting during the MS phase is assumed). At a given metallicity, this age marks the blue edge of the colour distribution of RGB stars. This phenomenon can be seen in Figure 3.7, where we show a comparison of various stellar evolution models in the region of the CMD where the tip luminosities start to drop out. Note that a variety of models were tested to see if the age parameter space was expanded - thus maximizing the number of stars with valid age assignments. However the models show reasonable agreement and similarity in this area of the CMD, as shown in that figure.

In cases where the position of the target star fell blueward than allowed by this

condition, an arbitrary age marker of 1 Gyr was assigned as an aid to interpreting the sample properties. Similarly, those redward of the oldest available track (18 Gyr) were assigned an age of 18 Gyr and a significant error assignment (discussed below).

As seen in Figure 3.8, roughly one third of the stars are below the 1.6 Gyr isochrone (implying younger ages). More detailed analysis of the age distribution and its implications are presented in §4.3, but it is quite obvious from this preliminary diagnostic that the sample contains a large number of young stars, of which the youngest appear to have preferentially formed in the bar field of the galaxy.

In order to check the impact of varying the [α/Fe] ratio, the same procedure was repeated with Victoria-Regina models that used [α/Fe]=0.0. As can be seen in Figure 3.9, the distribution normalizes slightly, but given the large errors in the estimated ages, we opted to stay with the original alpha enhanced models. The rationale for this was partly that there is little evidence to suggest that the stars in WLM have solar or lower [α/Fe] ratios, as is seen in some of the massive Local Group dSphs. More importantly, was that the calibration used in taking the Ca II equivalent widths onto the [Fe/H] scale, is based on galactic globular clusters which show on average, values close to [α/Fe]=+0.3 (Pritzl et al., 2005).

The technique used here for deriving ages can be applied successfully in globular cluster populations in the MW (Tolstoy, 2003), however studies using identical methods in dwarf galaxies have found it much more difficult to assign ages to evolved stars.

Tolstoy et al. (2003) first showed that the evolved stars in dSph galaxies often lay blueward or redward of the full age parameter space (See discussion in §3.3 Tolstoy et al. 2003; also Tolstoy 2003). This phenomenon has also been seen in the LMC Cole et al. (2005).

The question that we are left with is whether the bluest stars (those with inferred ages $\leq$1.6 Gyr) are really intermediate-mass stars on the early-asymptotic giant branch, or are true low-mass stars on the first-ascent RGB, influenced by uncertainties in composition or differential reddening. If the majority of the bluest stars *are* truly 1 Gyr or less, then we can look for concentrations of their more-evolved descendants (e.g., thermally-pulsing AGB stars). Amoung Local Group dwarfs, WLM has been found to have an extraordinarily large ratio of carbon- to M-stars, C/M= 12.4 ± 3.7 (Battinelli and Demers, 2004). This large population of carbon stars, along with the high recent star formation of WLM, does suggest that the majority of stars in the youngest age bin are truly young, and not first-ascent red giants for which the models are somehow invalid. Note that these stars are not likely to be differentially reddened AGB or RSG contaminants, as cross-correlation with UKIRT WFCAM *JHK* photometry rules this out. However, early-AGB stars ascending from the horizontal branch towards the thermally-pulsing (carbon star) phase can occupy the same CMD space as a bona fide RGB star, and this becomes quite likely in a composite population such as WLM's. If a given star picked off the RGB is in fact an early AGB star, at

a given metallicity the age of that star would be $\sim 30\%$ older than inferred here (for further discussion see Cole et al. 2005).

What physical processes may be present in the environment of a star in a dwarf galaxy, that are not found in globular clusters, and could account for the extreme CMD positions? Anomalous stellar rotation rates, mixing lengths or elemental enhancements in the stars in dwarf galaxies have been suggested as possible explanations (Tolstoy et al., 2003). It is not clear what affect these physical processes would have on stellar CMD position though, especially with respect to GGC calibrations, and current observational evidence to support these is lacking. Alternatively, internal differential reddening within WLM is a possibility. WLM itself is known to have non-trivial internal reddening contributions in addition to the line of sight reddening, which appears essentially constant over the survey range. Urbaneja et al. (2008) commented that their supergiant sample in WLM shows a mean reddening of E(B-V)=0.08, nearly twice as much as the line of sight Schlegel et al. (1998) foreground component commonly reported (E(B-V)=0.037). However it is unclear if this differential effect is enough to influence the ages to such extremes - and it is likely a combination of factors.

Figure 13 of Cole et al. (2005) quantitatively shows the age uncertainties introduced by several of these factors. Differential reddening clearly has the capability to shift and stretch the age distribution significantly. As the metallicity and age effects

counteract each other in color space near the TRGB, it is difficult to uniquely sample an old population in a dIrr, as even a uniform unbiased sample in (V-I) at this evolutionary locus will draw from a composite range of ages due to the entanglement in parameter space. Because of this fact, it is not surprising that there is a mix of old and young stars in the sample. However since we are primarily interested in evolved stars, we will examine ways to safely interpret our data in the framework of an asymmetric age distribution, as will be discussed in §4.3. And of course, despite the intriguing difficulty seen in assigning absolute ages to dwarf galaxy stars with this method, we seek primarily to constrain the *relative* ages of the stars in our WLM sample to aid in the interpretation of its evolution.

3.3.1 *Age Error Estimates*

Proper estimation of the uncertainties in these relative ages, must incorporate the dependence of photometric and spectroscopic uncertainties with respect to the target star's position in the theoretical plane. In order to accurately fold in both the photometric colour uncertainty ($\delta_{(V-I)} = 0.04$) and the uncertainty in the CaT metallicity measurements ($\sigma_{[Fe/H]} = 0.25$) the following algorithm was performed. Once the star was positioned in the age parameter space, the metallicity uncertainty was mapped into the error estimation by laying down four tracks of metallicity approximately $\pm 1\sigma_{[Fe/H]}$, and $\pm 1.5\sigma_{[Fe/H]}$ and of the best fit age, over the *original* full range of

age tracks. From there the photometric uncertainty shift could be applied to those minimum and maximum tracks, and a new interpolation at the extremes done. This provided us a way to explore how the uncertainties in age behaved as a function of age or metallicity. Figure 3.10 shows a visualization of the process.

Only stars that fell within the parameter space were considered when defining the uncertainty in age as a function of age. To this end, four representative average age values were created for the error estimation, and the stars in the full sample can be thought to have age uncertainties similar to these examples. Table 3.2 shows the adopted uncertainties. As expected the uncertainties grow with age, as both the resolution of the tracks, and behaviour of the metallicity changes are of great impact. These of course represent differential errors, i.e., within a set of adopted evolutionary tracks - systematic errors in how a particular model deals with a stars evolution up the giant branch can be sizeable and varied (Tolstoy et al., 2003).

In cases of either extreme age (i.e. star redward/blueward of age range) the stars are assigned errors based on the limits of the isochrone parameter space. As this analysis merely seeks differential ages for our population of stars, it was not necessary to conform with the maximum/minimum age values in previous studies (Tolstoy et al., 2003), and/or cosmological constraints. Stars blueward of the tracks, were arbitrarily given an age of 0.2 Gyr and errors were calculated using the above method for the range redward of the 1.6 Gyr track producing an upper error of $\sim$+1

Table 3.2. Age Error Values

Age [Gyr]	Lower Limit [Gyr]	Upper Limit [Gyr]	Adopted [Gyr]
0.2[a]	0.2	1.2	0.2^{+1}_{-0}
2	1	3	2^{+1}_{-1}
5	3	8	5^{+3}_{-2}
7	3	12	7^{+5}_{-4}
10	6	16	10^{+6}_{-4}
18[b]	10	18	18^{+0}_{-8}

[a]Stars that fell blueward of the 1.6 Gyr track were assigned a relative age of 0.2 Gyr to aid in analysis.

[b]These stars fell redward of the oldest track and were assigned this maximum age bin.

Gyr. The stars that fell outside the parameter space redward of the oldest tracks were given an age of 18 Gyr, and an age range of +0 and -8 Gyr respectively.

As mentioned, a reddening of E(B-V) = 0.035 for WLM was adopted from McConnachie et al. (2005). Variations in foreground reddening were examined by iteratively placing the position of the target stars onto the Schlegel et al. (1998) high resolution dust map. The results indicate that the foreground reddening does not vary, as the range is at most ΔE(B-V) $\leq$ 0.005 mag. Of course the possibility of differential reddening *within* WLM itself could contribute to the (V-I) position of stars in our age algorithm (as discussed with respect to Urbaneja et al. 2008). This represents the simplest explanation for why this technique may fail in extragalactic galactic populations, yet has minimal issues within our own MW galaxy when applied

to globular clusters. Internal differential reddening can be quantified using the Na I D line, however the calibrations from line width to E(B-V) may not be sensitive enough, and in any case the lines are not present in our spectral data. We should mention that Minniti and Zijlstra (1997), through radially segregated CMDs, argued against a dust gradient within WLM. However the possibility of small scale gas/dust structure leading to differential extinction on pc scales is still a possibility, and neutral hydrogen structure certainly shows evident for a turbulent ISM in localized pockets of WLM (Kepley et al., 2007). Some additional evidence for this substructure could be taken from the work of Jackson et al. (2006), who traced the polycyclic aromatic hydrocarbon (PAH) and hot dust emission in WLM, through the use of 8.0μm Spitzer data, and the nebular abundance work of Lee et al. (2005). Both of these works found some evidence of excess reddening on small scales near some of the H II regions in WLM.

While other astrophysical factors could impact the positions of the stars on the CMD (e.g., variations in relative internal reddening), we are unable to explicitly quantify these effects. Given those dependencies and the value of a typical metallicity error of $\pm$0.25 dex, the random error in age is $\sim \pm 50\%$.

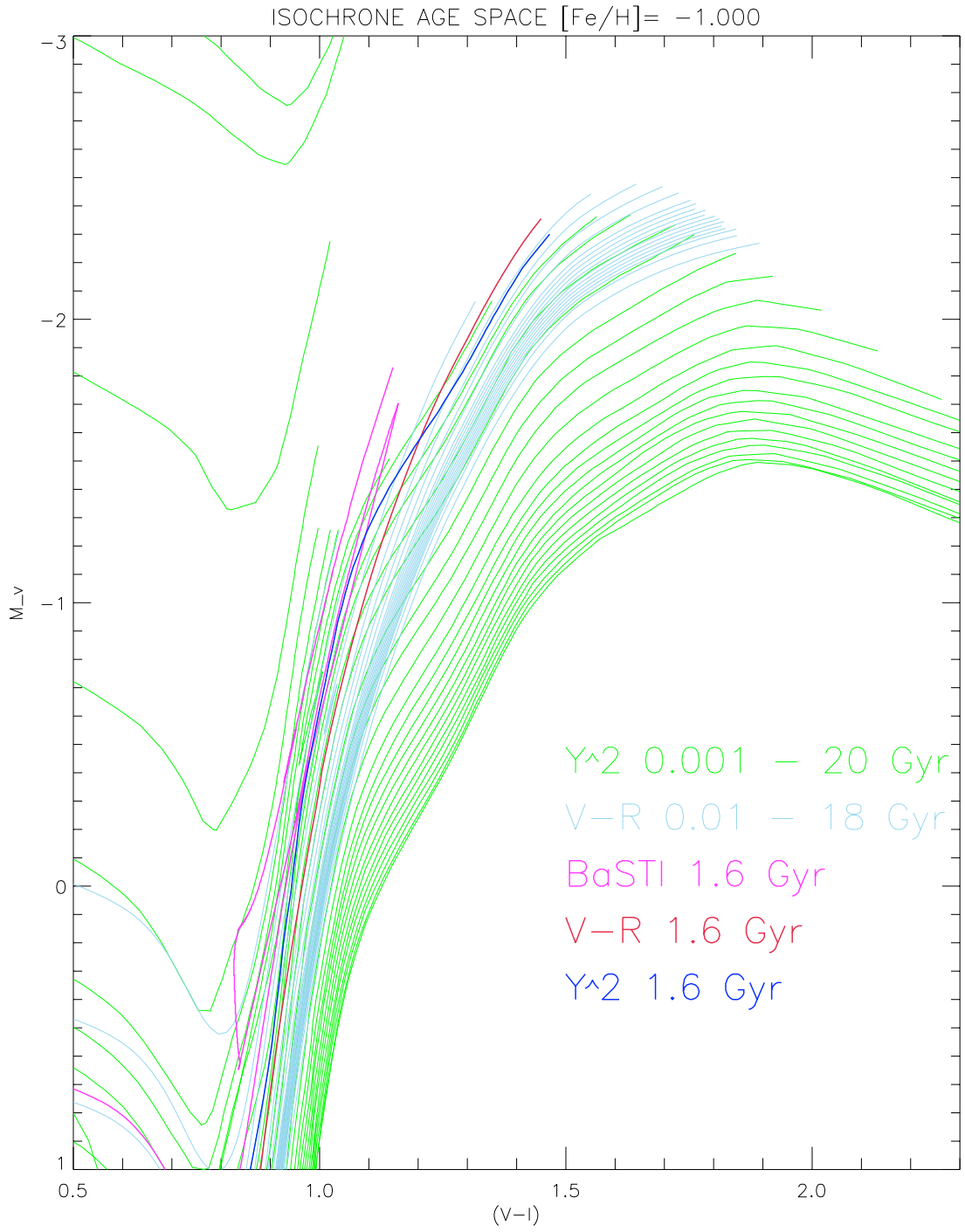

Figure 3.7: Comparison of various stellar evolutionary models with respect to our age analysis. The lower age limit of 1.6 Gyr in the age derivations is shown for a variety of these models at a metallicity of [Fe/H] = −1.0. The problematic stars that were too blue to be fit accurately, typically would be found at a locus similar to $(V\text{-}I)_0 = 1.2$, $M_V = -2.3$ in this example - where the track behaviour no longer allows for appropriate interpretation in any of the models (see text for discussion).

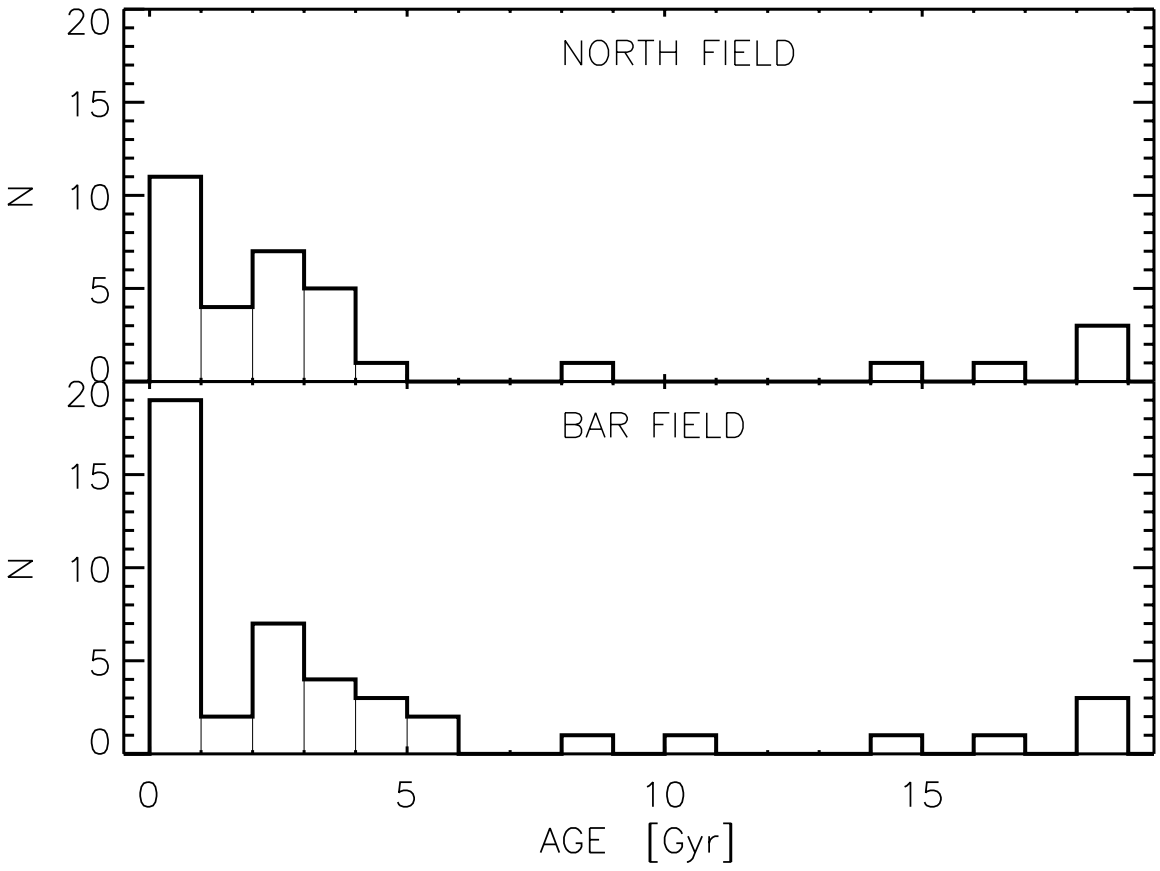

Figure 3.8: Age distribution for the North and Bar fields of WLM. A large number of stars in both fields fall in the youngest bin corresponding to stars bluer than the 1.6 Gyr track for the appropriate metallicity.

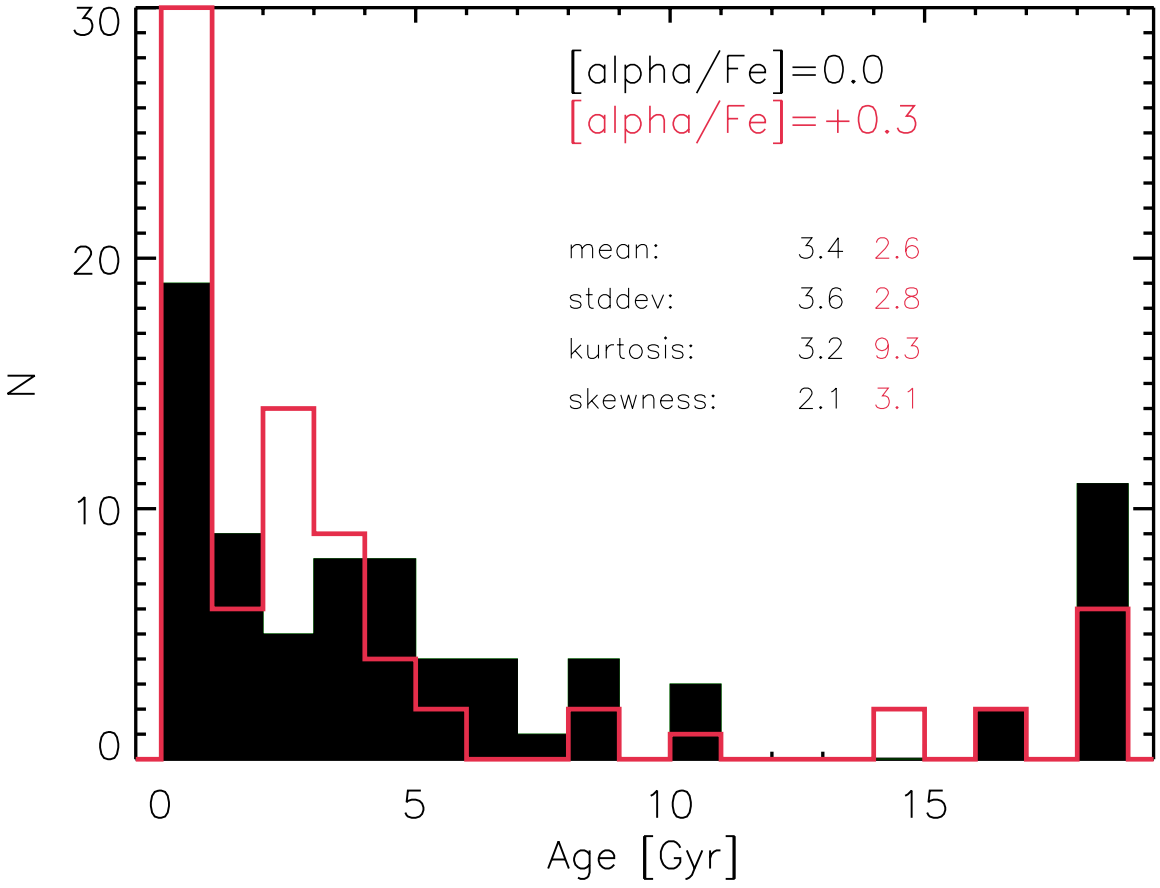

Figure 3.9: Test comparison of varying [α/Fe] for two possible values during the age derivations (see text for details). While not enough evidence in the literature is available to suggest that [α/Fe]=0 is more appropriate, there can be seen a minor change, with the distribution normalizing slightly.

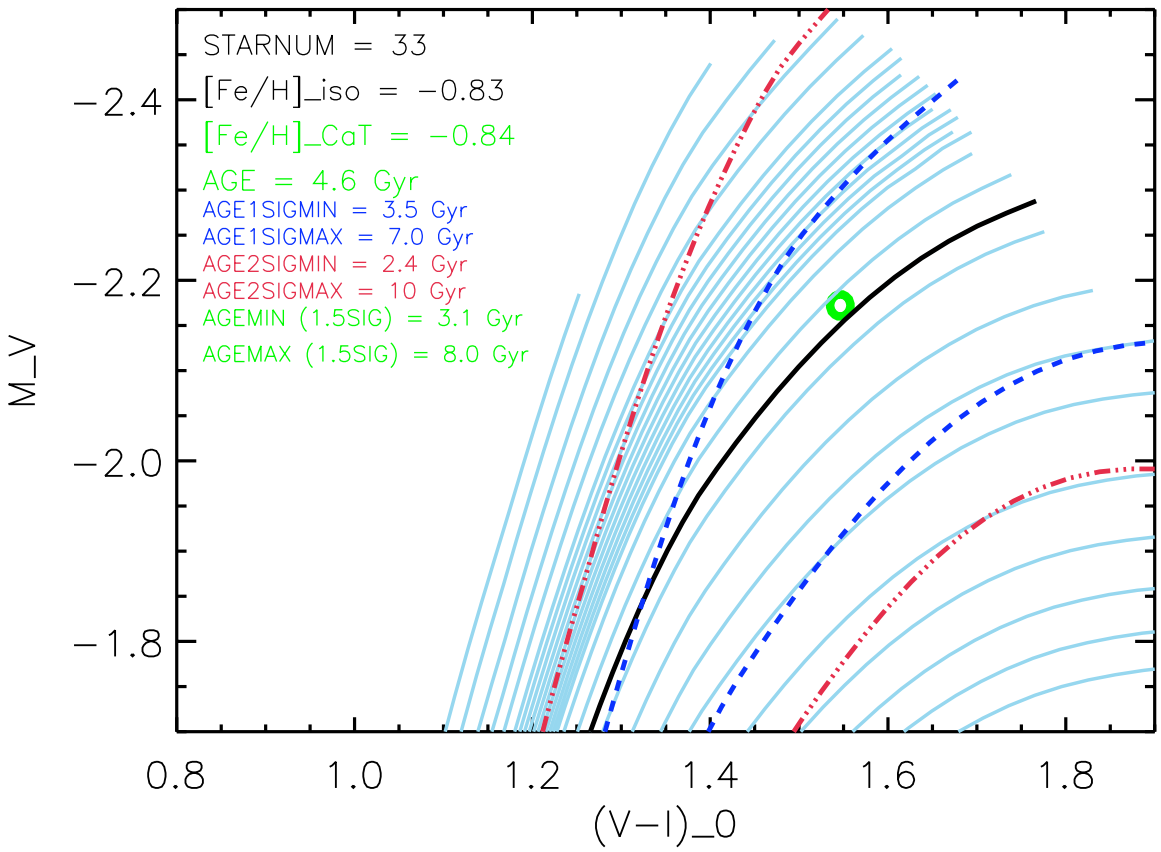

Figure 3.10: Example visualization of the error assignment for the ages. The star (*green circle*) is located closest to the 4.6 Gyr track (*solid black line*). Tracks of this age but with differing metallicities (*blue*, *red*) as discussed in the text, are laid down over the original metallicity and age parameter space (*cyan*), and shifted by the photometric uncertainty in colour. The lower and upper metallicity limit tracks are then interpolated within the framework of the original isochrones to provide a minimum and maximum age to take for the error in our age estimation.

Chapter 4

Analysis and Discussion of WLM

In this paper, we have determined the [Fe/H] and radial velocity values for 78 *individual* RGB stars in WLM. These can be used to examine the structure, kinematics, and chemical evolution history of this galaxy in conjunction with derived age estimates. This is unique, as all previous studies of supergiant stars (Venn et al., 2004; Bresolin et al., 2006; Urbaneja et al., 2008) and H II regions (Skillman et al., 1989; Hodge and Miller, 1995; Lee et al., 2005) sampled the young population and offer little insight into the earlier epochs of formation and evolution of this galaxy. Similarly, photometric studies (Minniti and Zijlstra, 1997; Hodge et al., 1999; McConnachie et al., 2005) were only able to provide global views of the metal poor population, and were subject to degeneracies in age and metallicity.

To begin the analysis, elliptical radii were computed for all of the stars in the sam-

ple as follows. The position angle of WLM was taken to be 181° (Jackson et al., 2004) and the eccentricity 0.59 (Ables and Ables, 1977). After transforming the equatorial coordinates into the transverse ξ, η plane, and calculating the axial components of the ellipse for a given star, the elliptical radius (r_{ell}) was determined from the geometric mean of the semi-major and semi-minor axes. These elliptical radii have uncertainties due to the inclination of WLM (69°, which is not assumed in the calculation; Ables and Ables 1977). In calculating these radii, an assumption is built in that the stars are in the geometric plane of WLM. A given star may of course sit off the major plane of the galaxy - thus the calculated elliptical radii have an intrinsic degeneracy with a star's true distance from the plane of the disk.

A summary of the spatial and photometric properties for the 78 RGB stars in this sample are listed in Table 4.1. This includes the metallicity, age, radial velocity, and elliptical radii values as well.

Table 4.1. Selected Parameters For WLM Stellar Sample

STARID	R.A. (degrees)	Dec. (degrees)	r_{ell} (degrees)	V (mag.)	I (mag.)	W_1 (Å)	W_2 (Å)	W_3 (Å)	$[Fe/H]_{CaT}$ (dex)	Δ[Fe/H] (dex)	V_{hel} (km s^{-1})	ΔV_{hel} (km s^{-1})	Age [a] (Gyr)
27626	0.5293	-15.5334	0.0978074	22.54	21.43	1.076	2.108	2.781	-1.62	0.21	-84	7	≤ 1.6
28986	0.4753	-15.5315	0.0889742	22.82	21.36	1.209	3.408	3.208	-0.91	0.26	-112	8	2.4
29674	0.4773	-15.5292	0.0857606	22.96	21.25	1.250	3.316	3.527	-0.79	0.27	-145	9	5.0
28080	0.4978	-15.5266	0.0814584	22.64	21.09	1.072	2.972	2.158	-1.51	0.22	-123	6	14.0
28895	0.4971	-15.5237	0.0775812	22.80	21.35	1.551	3.819	2.791	-0.80	0.27	-128	7	2.2
27491	0.5058	-15.5205	0.0747572	22.51	21.19	1.255	2.680	2.821	-1.36	0.23	-111	7	2.0
26541	0.4892	-15.5182	0.0702356	22.25	20.97	1.604	3.500	2.439	-1.16	0.25	-141	7	≤ 1.6
27842	0.4915	-15.5150	0.0661231	22.59	20.35	1.332	3.647	3.089	-0.89	0.27	-119	7	3.8
27409	0.4978	-15.5124	0.0630628	22.49	21.00	1.643	3.800	3.509	-0.62	0.28	-128	7	≤ 1.6
27569	0.4726	-15.5096	0.0620014	22.53	21.22	1.032	2.836	2.177	-1.59	0.21	-131	6	2.6
27916	0.4639	-15.5074	0.0626483	22.61	20.96	1.735	3.463	2.533	-1.00	0.25	-142	7	3.0
27018	0.4707	-15.5049	0.0569988	22.39	21.12	1.284	3.317	3.305	-1.09	0.25	-147	7	≤ 1.6
27845	0.4883	-15.4996	0.0461610	22.59	21.10	1.351	3.373	1.615	-1.48	0.22	-128	6	8.0
28137	0.5336	-15.4972	0.0606404	22.65	21.39	1.065	4.178	2.393	-1.02	0.26	-134	8	≤ 1.6
28441	0.5078	-15.4951	0.0435499	22.71	21.12	0.860	2.543	2.087	-1.73	0.20	-161	9	18.0
28427	0.4690	-15.4927	0.0435044	22.71	21.37	1.318	3.107	1.863	-1.46	0.22	-161	6	3.2

Table 4.1 (cont'd)

STARID	R.A. (degrees)	Dec. (degrees)	r_{ell} (degrees)	V (mag.)	I (mag.)	W_1 (Å)	W_2 (Å)	W_3 (Å)	$[Fe/H]_{CaT}$ (dex)	Δ[Fe/H] (dex)	V_{hel} (km s^{-1})	ΔV_{hel} (km s^{-1})	Age (Gyr) [a]
27310	0.4617	-15.4900	0.0449992	22.46	21.29	1.502	3.167	2.398	-1.26	0.24	-129	7	≤ 1.6
26940	0.4765	-15.4879	0.0342952	22.37	21.13	1.307	3.107	1.655	-1.63	0.22	-98	7	≤ 1.6
28333	0.4608	-15.4856	0.0416024	22.69	21.14	0.996	3.479	2.841	-1.12	0.25	-119	6	5.0
28970	0.5081	-15.4810	0.0277182	22.82	21.25	1.38	3.03	3.097	-1.02	0.25	-107	6	4.2
28881	0.5140	-15.4783	0.0293921	22.80	21.31	1.269	3.353	3.056	-0.97	0.26	-120	7	3.4
27265	0.5193	-15.4758	0.0320861	22.45	21.34	1.295	3.567	2.699	-1.10	0.25	-116	6	≤ 1.6
27427	0.4687	-15.4737	0.0260121	22.49	21.75	0.971	1.304	0.962	-2.55	0.13	-109	9	≤ 1.6
27926	0.4824	-15.4713	0.0129957	22.61	21.00	1.505	3.346	2.603	-1.09	0.25	-123	6	4.6
28395	0.4847	-15.4689	0.0091797	22.70	21.41	1.213	3.563	1.996	-1.30	0.24	-139	6	2.4
26678	0.5100	-15.4664	0.0190786	22.29	21.40	0.977	3.412	2.772	-1.28	0.25	-129	5	≤ 1.6
27833	0.5018	-15.4641	0.0106341	22.59	21.68	1.572	3.131	3.069	-0.99	0.25	-124	6	≤ 1.6
27429	0.5069	-15.4616	0.0160755	22.49	21.13	1.703	3.674	3.058	-0.79	0.27	-123	7	≤ 1.6
28322	0.4653	-15.4592	0.0269871	22.69	20.90	1.640	2.952	2.410	-1.23	0.23	-114	6	16.0
27407	0.5182	-15.4567	0.0287657	22.49	21.11	1.358	3.259	2.033	-1.40	0.23	-133	7	2.8
28405	0.5148	-15.4545	0.0267520	22.70	21.18	1.132	2.586	2.590	-1.46	0.22	-128	6	10.0
27044	0.5086	-15.4494	0.0258708	22.40	21.24	1.241	3.385	2.467	-1.27	0.24	-132	6	≤ 1.6

Table 4.1 (cont'd)

STARID	R.A. (degrees)	Dec. (degrees)	r_{ell} (degrees)	V (mag.)	I (mag.)	W_1 (Å)	W_2 (Å)	W_3 (Å)	$[Fe/H]_{CaT}$ (dex)	Δ[Fe/H] (dex)	V_{hel} (km s^{-1})	ΔV_{hel} (km s^{-1})	Age (Gyr) [a]
28316	0.5162	-15.4466	0.0338115	22.69	21.28	1.241	3.385	2.467	-0.99	0.25	-111	6	≤ 1.6
26856	0.4692	-15.4438	0.0344805	22.35	20.94	1.991	4.473	3.291	-0.38	0.31	-115	6	≤ 1.6
27091	0.4726	-15.4410	0.0354185	22.41	21.25	1.273	3.422	2.340	-1.29	0.24	-130	6	≤ 1.6
28220	0.4741	-15.4387	0.0372675	22.67	21.17	0.903	3.485	2.757	-1.18	0.25	-145	6	4.2
27342	0.5131	-15.4361	0.0424025	22.47	21.09	1.040	3.951	2.198	-1.22	0.25	-141	5	1.8
28371	0.5223	-15.4334	0.0506345	22.70	21.31	1.122	2.208	1.219	-2.05	0.17	-109	6	18.0
28056	0.5086	-15.4305	0.0469298	22.63	21.28	1.263	3.507	3.106	-0.94	0.26	-130	6	≤ 1.6
27590	0.5008	-15.4281	0.0476470	22.53	21.16	1.048	3.247	2.778	-1.24	0.24	-126	7	2.9
27004	0.5074	-15.4248	0.0534145	22.39	21.22	1.518	3.831	3.092	-0.82	0.27	-107	9	≤ 1.6
27856	0.5229	-15.4224	0.0627850	22.59	21.13	1.721	3.454	2.367	-1.07	0.25	-98	8	1.8
27548	0.4668	-15.4210	0.0611249	22.52	21.20	1.716	3.654	3.285	-0.71	0.28	-149	7	≤ 1.6
28328	0.5189	-15.4199	0.0637268	22.69	21.06	1.682	4.416	2.915	-0.55	0.29	-156	6	≤ 1.6
28682	0.4792	-15.4188	0.0599319	22.76	21.43	0.787	3.122	2.674	-1.35	0.23	-116	8	3.5
31087	0.4885	-15.4176	0.0603162	23.21	21.47	0.996	2.930	2.110	-1.42	0.21	-133	6	18.0
27765	0.4819	-15.4161	0.0628594	22.57	21.41	1.439	2.975	1.982	-1.46	0.22	-144	6	≤ 1.6
28590	0.4775	-15.4118	0.0691717	22.75	21.13	1.329	3.127	2.235	-1.32	0.23	-148	6	14.0

Table 4.1 (cont'd)

STARID	R.A. (degrees)	Dec. (degrees)	r_{ell} (degrees)	V (mag.)	I (mag.)	W_1 (Å)	W_2 (Å)	W_3 (Å)	$[Fe/H]_{CaT}$ (dex)	Δ[Fe/H] (dex)	V_{hel} (km s^{-1})	ΔV_{hel} (km s^{-1})	Age (Gyr) [a]
27189	0.4786	-15.4095	0.0719565	22.44	21.26	1.509	3.021	2.529	-1.27	0.24	-130	6	≤ 1.6
26226	0.5257	-15.4046	0.0845370	22.13	20.84	1.456	2.996	2.437	-1.41	0.23	-103	6	≤ 1.6
28196	0.4656	-15.4022	0.0843228	22.66	21.26	0.946	3.665	2.272	-1.27	0.24	-115	6	4.2
28736	0.4630	-15.3996	0.0883728	22.77	21.25	1.082	3.432	1.590	-1.51	0.22	-137	6	18.0
28821	0.5198	-15.3966	0.0920141	22.79	21.51	1.067	3.489	1.903	-1.38	0.23	-139	8	2.4
29499	0.5074	-15.3936	0.0928048	22.92	21.41	1.078	2.906	1.921	-1.54	0.21	-118	6	18.0
27734	0.5055	-15.3913	0.0954310	22.57	21.28	1.539	2.910	1.823	-1.51	0.21	-123	7	1.8
29590	0.4825	-15.3878	0.0992865	22.94	21.49	1.346	4.305	2.224	-0.86	0.27	-130	9	2.8
27667	0.4857	-15.3850	0.1026929	22.55	21.30	0.789	3.592	2.271	-1.38	0.24	-153	6	≤ 1.6
27192	0.4952	-15.3816	0.1069359	22.44	21.00	1.148	2.765	1.947	-1.68	0.21	-107	8	3.8
27515	0.5155	-15.3759	0.1168678	22.51	20.92	1.806	3.416	3.241	-0.78	0.27	-124	6	1.8
28531	0.4731	-15.3737	0.1185451	22.73	21.15	1.946	3.563	2.593	-0.84	0.26	-127	6	2.6
28064	0.5206	-15.3691	0.1266431	22.64	21.42	1.198	2.689	2.413	-1.48	0.22	-126	6	≤ 1.6
19203	0.5036	-15.3643	0.1298484	24.05	21.47	0.970	2.766	1.639	-1.42	0.19	-189	7	18.0
16415	0.5188	-15.3616	0.1356525	22.59	21.21	1.645	3.217	2.266	-1.21	0.24	-117	5	2.0
16348	0.4626	-15.3572	0.1414459	22.52	21.06	1.378	4.115	2.913	-0.79	0.28	-149	6	1.8

Table 4.1 (cont'd)

STARID	R.A. (degrees)	Dec. (degrees)	r_{ell} (degrees)	V (mag.)	I (mag.)	W_1 (Å)	W_2 (Å)	W_3 (Å)	$[Fe/H]_{CaT}$ (dex)	Δ[Fe/H] (dex)	V_{hel} (km s^{-1})	ΔV_{hel} (km s^{-1})	Age (Gyr) [a]
16163	0.5051	-15.3542	0.1430462	22.30	21.10	1.103	3.501	2.765	-1.21	0.25	-146	6	≤ 1.6
16218	0.5013	-15.3490	0.1494224	22.38	21.11	1.325	3.064	2.466	-1.36	0.23	-144	6	≤ 1.6
16335	0.5224	-15.3465	0.1555663	22.51	21.22	0.667	2.320	0.911	-2.32	0.16	-148	6	3.2
16326	0.5105	-15.3438	0.1570543	22.50	21.12	1.017	2.970	1.857	-1.67	0.21	-111	7	3.2
16329	0.4811	-15.3393	0.1619626	22.50	21.30	1.208	2.929	2.136	-1.52	0.22	-140	6	≤ 1.6
16225	0.4775	-15.3361	0.1663648	22.39	21.21	0.629	3.286	1.653	-1.79	0.21	-130	5	≤ 1.6
16511	0.5299	-15.3321	0.1753224	22.69	21.23	0.760	3.408	1.502	-1.68	0.21	-148	6	8.0
16354	0.4947	-15.3299	0.1738444	22.53	21.21	0.797	3.207	1.974	-1.61	0.21	-162	6	2.6
16298	0.4728	-15.3269	0.1786507	22.46	21.09	1.175	3.025	2.082	-1.53	0.22	-144	6	2.6
16413	0.4822	-15.3213	0.1852281	22.59	21.13	1.197	3.741	2.747	-1.02	0.26	-132	7	1.8
16474	0.5200	-15.3183	0.1910044	22.65	21.11	0.867	2.697	1.853	-1.77	0.20	-130	5	16.0
16299	0.5024	-15.3144	0.1941447	22.46	21.07	0.731	3.259	2.277	-1.53	0.23	-151	5	3.2
16259	0.4855	-15.3111	0.1982649	22.43	21.04	0.937	3.042	2.702	-1.40	0.23	-151	6	2.7
16300	0.5033	-15.3084	0.2019618	22.46	21.20	1.605	2.852	2.630	-1.26	0.24	-147	9	≤ 1.6

[a]Derived ages were cutoff artificially at 1.6 Gyr as the interpolation of the model space became uncertain below this age. Stars following below this were assigned an age of 0.2 Gyr to aid in interpretation of the sample.

4.1 Chemistry

The metallicity distribution function from the full sample of stars provides the first detailed insight into the chemistry of the evolved population of WLM. The top panel of Figure 4.1 shows the MDF for the WLM sample subdivided into the bar and north fields. The global mean (-1.28 ± 0.03, $1\sigma = 0.37$)[1] and peak (~ -1.30) values of the MDF are slightly higher than the photometric determinations, but consistent within errors. For example, Hodge et al. (1999) derived [Fe/H] $= -1.51 \pm 0.09$ by isochrone fitting to the lone GC in WLM; McConnachie et al. (2005) found [Fe/H] $=-1.5 \pm 0.2$ (assuming no alpha-element enhancements) from empirically calibrated RGB colours. Minniti and Zijlstra (1997) found [Fe/H] $= -1.45 \pm 0.2$, again from the photometric properties of the RGB. These photometric metallicity estimates essentially give lower limits, as younger stars will be shifted bluer on the RGB. Our higher results confirm that effect - as shown by our higher metallicities and range of ages for this composite population.

[1]It should be noted our observed spread in metallicities should be compared to the intrinsic uncertainty in obtaining our individual [Fe/H] estimates (i.e., Δ[Fe/H]=$\pm$0.25 dex)

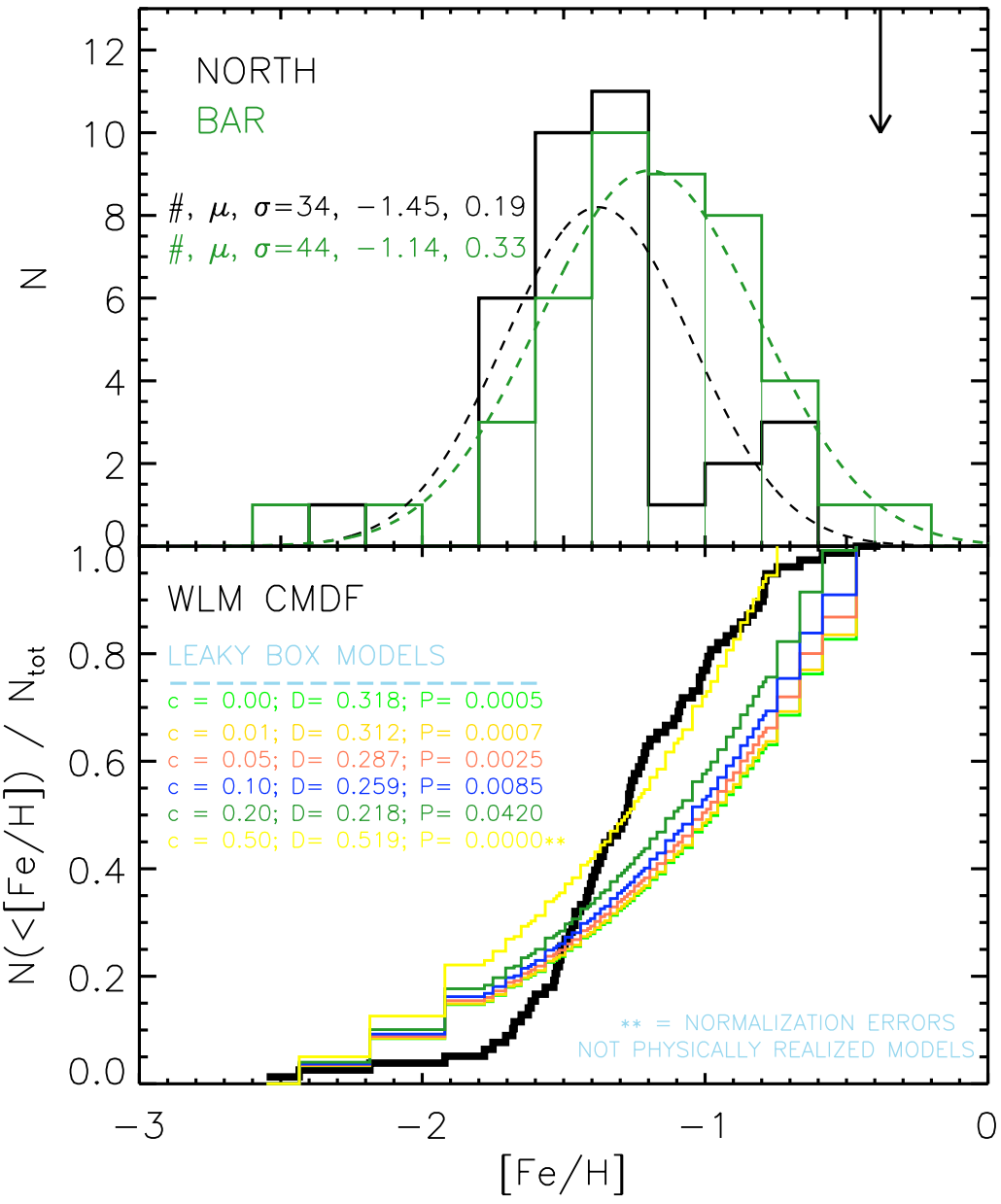

Figure 4.1: The metallicity distribution function for the two FORS2/MXU fields in WLM (*top panel*). The bin size is 0.2 dex, and fitted Gaussians with parameters shown are indicated by the dashed lines. Note that the mean values for the two fields differ by ~ 0.3 dex, and there is an absence of extremely or even moderately metal poor stars in either field. The [Fe/H] estimates from the Venn et al. (2003) supergiants are shown by the solid arrow. The cumulative metallicity distribution function (unbinned) for the WLM sample is shown in the bottom panel. The coloured lines represent cumulative distributions for simple leaky box chemical evolution models with different values (c) controlling the effective yield. Corresponding Kolmogorov-Smirnov D-statistics (D), and probabilities (P) are shown as well.

These metallicities may be compared to star formation history solutions derived from analyses of CMDs over various spatial location in WLM by Dolphin (2000) and Mateo (1998). Those studies reach deep enough to provide accurate SFH solutions in WLM at a fine time resolution, and have some spatial information allowing for a comparison to our multi-field sample. Both studies indicate that the most recent star formation has occurred in the inner parts of the galaxy (see Dolphin 2000, Fig. 7; Mateo 1998, Fig. 8a), again consistent with our findings in a relative decrease in metal rich stars in the outer field of the galaxy.

In Dolphin (2000), solutions for the metallicity evolution after the first 3 Gyr star formation episode suggest that populations forming 7-9 Gyr ago would have come from material with an initial enrichment of $[\mathrm{Fe/H}]_0 = -1.34 \pm 0.14$. Even younger stars that formed $\sim$ 3 Gyr ago, are predicted to have been born out of material with $[\mathrm{Fe/H}]_0 = -1.20 \pm 0.14$ dex. These values are both in excellent agreement with our peak and median values for the WLM metallicity distribution, which sampled an intermediate age population with a similar age spread (1-12 Gyr). While details of the first epochs of SF are not well sampled from the CMDs (who do not reach the MSTO), the photometry does reach to the HB allowing for more accurate SFH solutions for the past few Gyr. Table 4.2 has a comparison of values for representative age populations in this study and the Dolphin (2000) work. It should be kept in mind that the HST field of view in that work covers only a small fraction of the galaxy.

Table 4.2. Comparison to SFH Age-Metallicity Solutions

Age[a][Gyr]	SFR[a][$10^{-5} M_{\odot}\mathrm{yr}^{-1}$]	$[\mathrm{Fe/H}]_0$[a]	Age bin[b][Gyr]	$[\mathrm{Fe/H}]_{CaT}$[b]	$\langle$ t $\rangle$[b][Gyr]	N_{bin}
0 – 1	27 ± 6	-1.08 ± 0.18	≤ 1	-1.25 ± 0.03	0.2	58
1 – 2.5	37 ± 8	-1.13 ± 0.16	...	...		
2.5 – 5	8 ± 8	-1.20 ± 0.14	1 – 6	-1.33 ± 0.07	3.2	14
5 – 7	13 ± 15	-1.25 ± 0.13	...	...		
7 – 9	27 ± 25	-1.34 ± 0.14	...	...		
9 – 12	67 ± 15	-2.18 ± 0.28	≥ 10	-1.44 ± 0.10	11.2	6

[a]From Dolphin (2000)

[b]This work

The narrowness of our [Fe/H] distribution for the evolved population is perhaps unexpected, given that WLM has such an extended SFH (Dolphin, 2000), and range of ages at the tip of the RGB. Low mass stars might take 10 Gyr or longer to arrive at the TRGB, while the most massive stars at that evolutionary locus could have formed many Gyr later from metal enriched gas. However, even with the bin sizes of 0.2 dex, a sharp cutoff at [Fe/H] $\simeq$ -1.8 is visible in both fields (recall Figures 3.4, 4.1). Dolphin (2000) suggested that there was a significant star formation event 9-12 Gyr ago with an enrichment up to $[\mathrm{Fe/H}]_0 = -2.18 \pm 0.28$, however those stars do not appear in our sample in great number.

Although significantly different environmental characteristics exist in dSphs, Helmi et al. (2006) studied the absent low metallicity tail in four of those local group satellites. In that work the absent MP populations were stars with [Fe/H] $\leq$-3.0 dex. The

key in this comparison is not the absolute low metallicity edge of the MDFs in Helmi et al. (2006), but the shape of the lower 10-20% of the distribution - which shows a sharp dropoff when compared with the slowly varying MW halo metal poor distribution (see e.g. their Fig. 3). The Helmi et al. (2006) work ultimately concluded that a late formation time, or pre-enrichment of the gas, was necessary to explain the dearth of extremely metal poor stars.

If dIrr galaxies are related in some way to dSph, particularly with respect to when the bulk of their star formation occurred relative to the epoch of reionisation (i.e. "survivors" vs. "fossils"; Ricotti and Gnedin 2005), then a direct comparison of the metal poor tails is critical. While normalization to the Hamburg/ESO Survey halo data (Beers and Christlieb, 2005) is difficult due to the metallicity offset, a qualitative look at our cumulative MDF (Figure 4.1) clearly shows no smoothly decaying metal poor tail to WLM's [Fe/H] distribution, but a sharper edge like the Helmi et al. (2006) dSph samples. It should be noted that the Hamburg/ESO CMDF used in the Helmi et al. (2006) dataset has since been bias corrected, providing better agreement with at least Fornax dSph (Schoerck et al. 2008, Evan Kirby; priv. communication). We however do not have the sample numbers to do any sort of quantitative comparison to the dSph MDFs.

In order to quantify the probability that the metallicities in our sample are drawn from a Gaussian parent distribution, a Kolmogorov-Smirnov (K-S) test was performed

on the cumulative metallicity distribution function (CMDF). The probability that the distribution is Gaussian is $\sim 8 \times 10^{-19}$. More interesting is a comparison to a metallicity distribution predicted by a simple closed or leaky box chemical evolution model. The bottom panel of Figure 4.1 shows our cumulative metallicity function compared to predicted distributions from leaky box models with a range of parameters. The K-S probabilities that our distribution is drawn from one of the simple one zone models is $\leq 4\%$ for all models shown. Our distribution again shows a lower number of metal poor stars compared to these models. The low metallicity dropoff is primarily due to observational difficulties in attempting to sample a sizeable relative number of low [Fe/H] stars. Metal poor stars at this evolutionary locus are difficult to find in any galaxy due to a population bias resulting from mass dependent stellar evolutionary timescales.(c.f. Cole et al. 2008). For a given time interval, more young, high mass, high metallcity stars will evolve through the RGB than older, low mass, metal poor stars in the same time interval. The dominant fraction of young stars at the RGB is large enough to outnumber the metal poor old stars, despite the contradicatory initial relative numbers of the IMF. This effect will be enhanced in the presence of any age-metallicity relationship and is still present for non-simple populations with extended SFHs like WLM.

The high metallicity tail of the MDF also offers some comparison to the intriguing abundance analysis of past nebular and stellar studies (e.g. Venn et al. 2003; Lee et al.

2005; Bresolin et al. 2006; Urbaneja et al. 2008). The Venn et al. (2003) results for two A5 Ib supergiants had a derived metallicity of [Fe/H] = -0.38 ± 0.20 dex, and one had an oxygen abundance of [O/H] = -0.21 ± 0.10 (WLM-15). Analysis of three early B supergiants (Bresolin et al., 2006) indicated mean oxygen values of [O/H] = -1.0, -0.8, and -0.8 dex for their sample, providing some estimate of the chemistry of WLM's young population. While the recent study by Urbaneja et al. (2008) found a mean metallicity of [Z] = -0.87 ± 0.06 dex, but one object with an abundance similar to the WLM-15 result of Venn et al. (2003). Due to the extended SFH of WLM, it is expected that this RGB sample is drawn from a composite population with a sizeable age range. As such, we might expect to see some higher metallicity, higher mass stars that formed at later times from enriched material and evolved more quickly to near the tip of the RGB. The enrichment level of the Venn et al. (2003) supergiants is shown by the vertical arrow in the top panel of Figure 4.1. Few of the stars in the WLM sample are at the metallicities of these supergiants.

Not surprisingly, the young, enriched stars that we do see, are found preferentially in the bar field of WLM (see Figure 4.1 top panel). Several tracers of high active SF are observed in this inner field, notably the strong and numerous H II regions (Hodge and Miller, 1995; Youngblood and Hunter, 1999) consistent again with the most enriched material being found in the central body of the galaxy.

This is more clearly visualized in the top panel of Figure 4.2, where the mean

metallicity decreases by ∼0.3 dex with distance from the galactic core. From that figure we find a radial metallicity gradient of $\frac{\partial[Fe/H]}{\partial r} = -0.14 \pm 0.02$ dex/kpc. This smooth gradient may however be a line of sight superposition of two (or more) spatially localized subpopulations, mimicking a smooth radial profile.

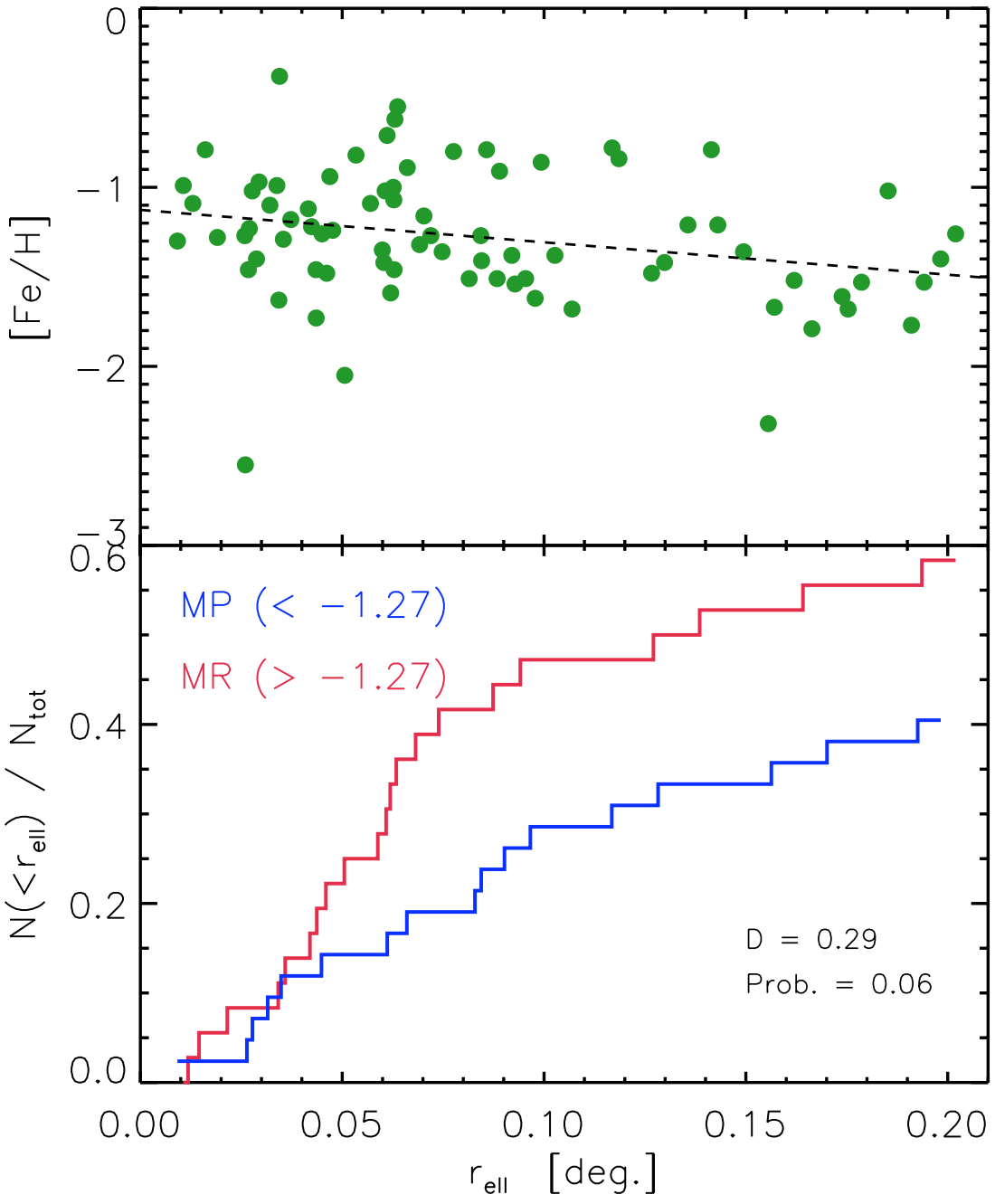

Figure 4.2: [Fe/H] vs. elliptical radii for the full sample of RGB stars in WLM (*top panel*). A radial change is clearly evident, and quantitatively confirms the interpretation of the disk of WLM being a region of higher SF in more recent times relative to the outer galactic regions. Cumulative distribution functions vs. elliptical radii for the metal rich and metal poor subsamples (*bottom panel*). The metal poor half of the sample rises more linearly over the radial extent of our survey, compared to the more centrally concentrated metal rich subpopulation.

This population change is consistent with the results from the photometric study by Minniti and Zijlstra (1997). The [Fe/H] values show a dispersion in metallicity that is roughly constant over the sampled region of the galaxy ($\sigma = 0.32$), similar to previous analyses. A two sided Kolmogorov-Smirnov test of the bar and north field cumulative metallicity distributions reveals that they have a very small probability of being drawn from the same parent distribution ($P = 0.005$). Splitting the sample into those stars with $r_{ell} \leq 0.1$ deg. and $r_{ell} > 0.1$ deg. and running the same K-S test, results in a similar probability ($P = 0.024$). This would appear to strengthen the interpretation of distinct spatial populations in WLM, as the inner and outer CMDFs show statistically different properties - not just different mean metallicities.

The bottom panel of Figure 4.2 shows the cumulative radial number density (CDF) of metal poor and metal rich stars as a function of elliptical radius from the center of WLM. The metal poor stars are found in more uniform numbers independent of radial position within the galaxy, whereas the more metal enhanced stars are found preferentially closer to the center of WLM.

In Figure 4.3 the unbinned cumulative metallicity distribution functions (CMDFs) are shown for three age divisions of our sample. In each bin, the WLM subsample is compared to predicted CMDFs from a leaky, and closed box chemical evolution model. While our sample deviates from the simple models in the youngest age bins, the oldest age bin ($t > 6$ Gyr) shows a large probability of being drawn from a

distribution approximated by the closed box model. We might naively expect that the oldest stars would have a characteristic shape to their metallicity distribution that would be more closely approximated by a closed box scenario. The deviations at younger ages, may be partially the result of an increase of accreted gas, and as such, the CMDF of the younger stars begins to vary from the shape predicted by a closed box model. However a simpler astrophysical explanation is also contributing. As mentioned earlier, the evolutionary flux through the RGB results in higher numbers of young stars in that locus than older, low mass, metal poor stars. This effect means that our 78 star sample is a slightly skewed example of the true [Fe/H] distribution at the TRGB. As such, the probabilities found in the K-S tests are really describing how our *sample* is comparing to the closed box models - presumably the true metallicity distribution of WLM would have more metal poor stars, and the K-S probabilities would be higher. This popluation bias is much more prominent in the youngest age bin, and at the older bin, less of a factor, and so these stars may result in a more representative sample of WLM's metallicity distribution. With larger numbers of stars it may be possible to quantify how much of the probability change with age is due to an evolutionary population bias, and how much may be attributed to infall of pristine gas.

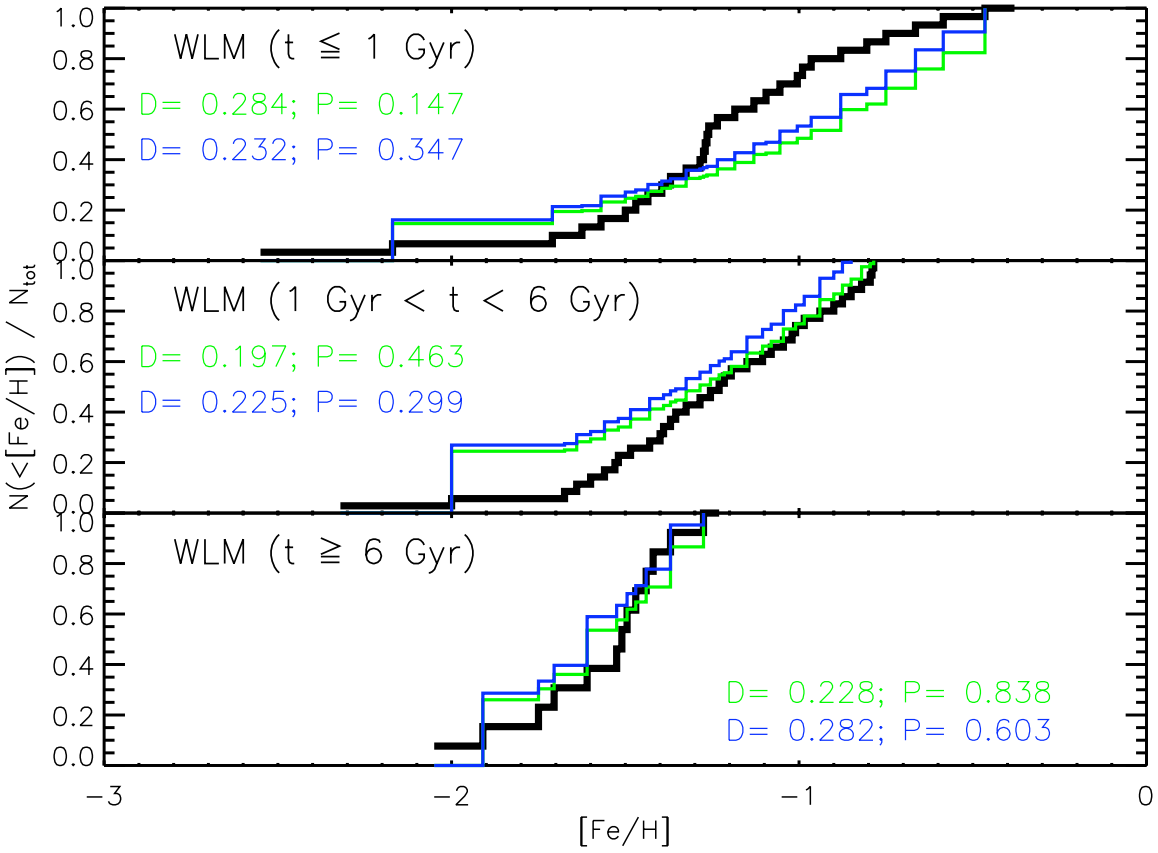

Figure 4.3: Cumulative metallicity distributions for the WLM sample, subdivided by ages: $t < 1$ Gyr (*top panel*), $1 \leq t \leq 6$ (*middle panel*), $t > 6$ Gyr (*bottom panel*). Comparison CDFs based on simple closed (*green*), and leaky box (*blue*) chemical evolution models are shown for each age set. The two sided Kolmogorov-Smirnov statistics are shown, as well as the probability that our metallicity distributions are drawn from one of the theoretical distributions. The probability rises steeply with age for the closed box model, with $P \sim 14\%, 46\%, 84\%$ in the three bins.

4.2 Chemodynamics

Figure 4.4 shows the results of the radial velocity analysis, presented as two velocity distribution functions (VDFs) for the bar and north field. Each field has been further subdivided into metal poor and metal rich subsamples. Of note are the peaked, Gaussian, distributions around the mean values of $\langle v_{north} \rangle = -136 \pm 3$ km s^{-1} and $\langle v_{bar} \rangle = -126 \pm 3$ km s^{-1} for the north and bar field samples respectively. Comparing these subsamples shows that the *mean velocities* of the north and bar, metal poor and metal rich, populations are consistent (i.e., $\langle v_{NMP} \rangle = \langle v_{NMR} \rangle = -136 \pm 3$ km s^{-1}; $\langle v_{BMP} \rangle = \langle v_{BMR} \rangle = -126 \pm 4$ km s^{-1}). This indicates that the general bulk motion of both subgroups of stars in a given field holds in accordance with the group mean. However the *velocity dispersions* of the metallicity subpopulations, do not show the same uniform characteristics. The velocity dispersions of the metal poor subsamples for the north and bar fields are larger than the metal rich samples in both fields. We find: $\sigma_{v(NMP)} = 19$ km s^{-1}, $\sigma_{v(NMR)} = 12$ km s^{-1}, $\sigma_{v(BMP)} = 20$ km s^{-1}, and $\sigma_{v(BMR)} = 14$ km s^{-1}. The Sculptor dSph galaxy (Tolstoy et al., 2004) shows similar chemodynamic trends.

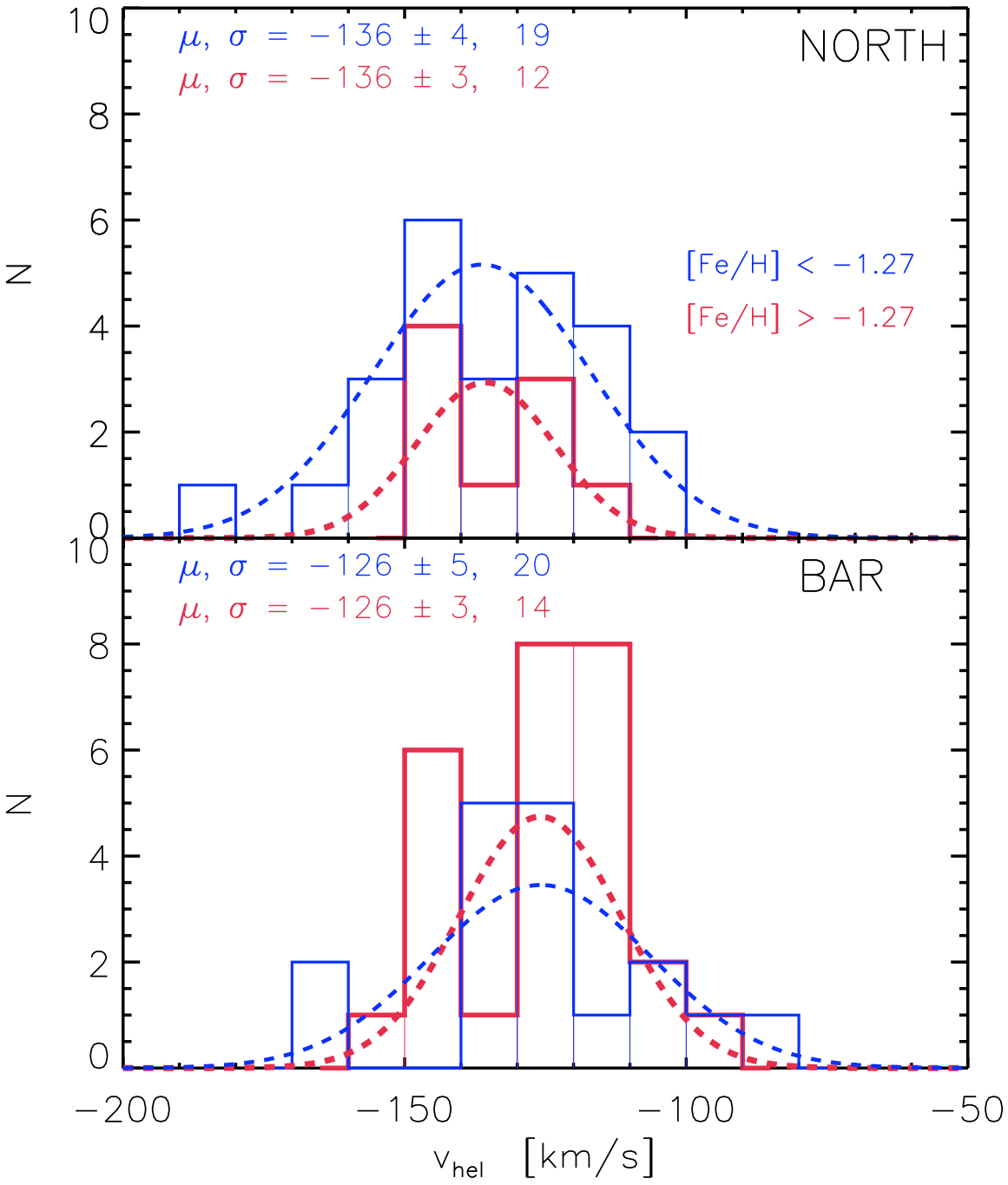

Figure 4.4: Velocity distributions for metallicity segregated subsamples in the north field (*top panel*), and the bar field (*bottom panel*). The average metallicity and dispersion values from the Gaussian fits (*dashed lines*) are shown for all stars in each field near the top of each panel. The mean uncertainty for each heliocentric corrected radial velocity value was ± 6 km s^{-1}.

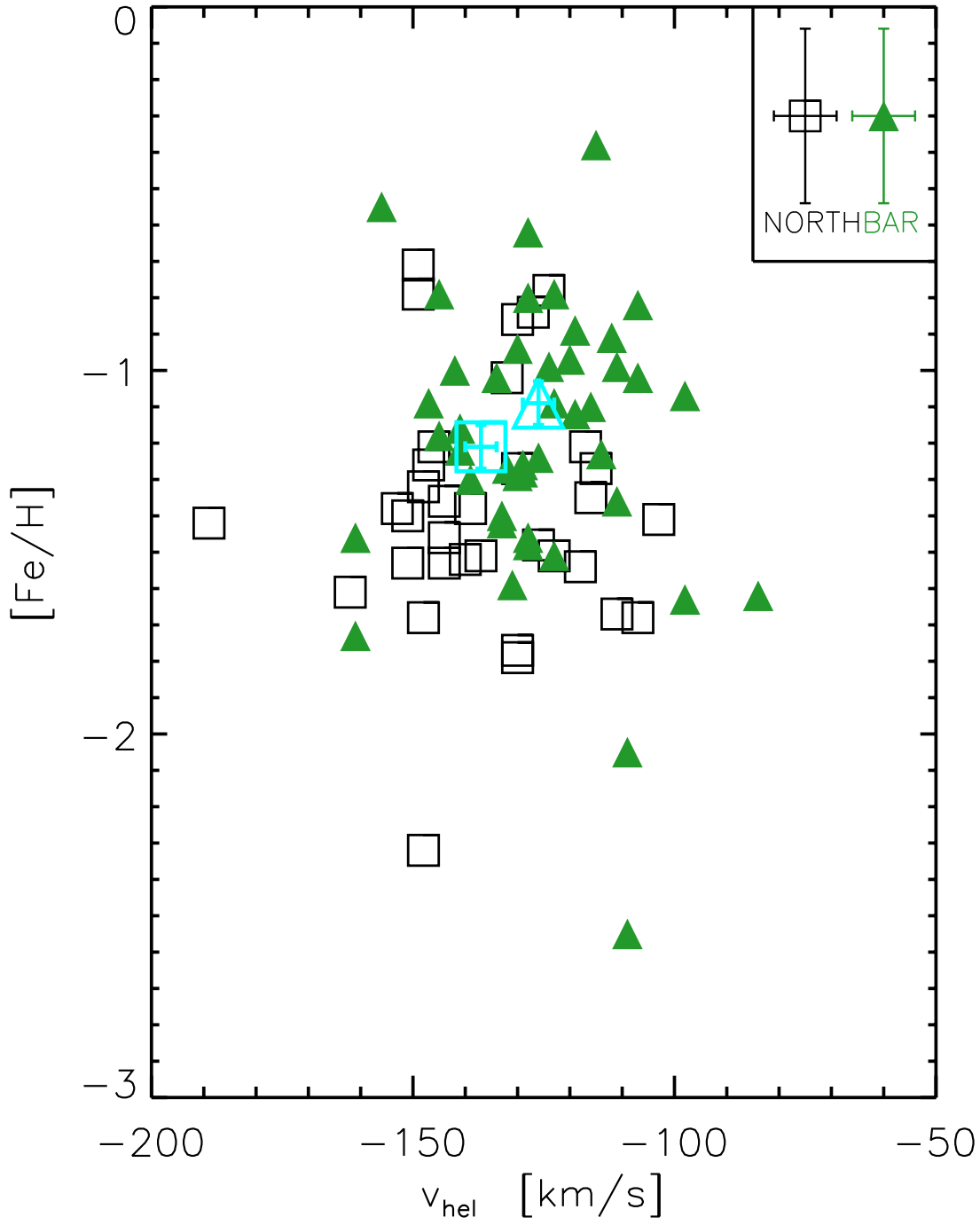

Figure 4.5: Plot of the heliocentric velocity and metallicity of the 78 RGB stars in the two WLM fields. The mean bar(*green triangles*) and north (*open squares*) field values are noticeably offset in both chemical and velocity space (*cyan symbols*). Errors are ±0.25 dex, and ±6 km s^{-1} respectively per star, and shown for comparison on the simulated legend points at the top.

Figure 4.5 again illustrates that the velocity and metallicity of the stars in the WLM sample are changing with respect to position in the galaxy. The north field stars are more metal poor and have a higher approach velocity relative to the bar field stars. This chemodynamic signature is consistent with the interpretation of previous photometric studies that found a population gradient in WLM. However, our results separate the metallicity-velocity-position degeneracies, and we have also determined ages. What more can these detailed results offer in understanding the star formation history, variation in the stellar populations, and overall chemodynamical evolution in WLM?

4.3 Properties of Each Stellar Population

The sample is divided into three age bins to examine the means and dispersions of the metallicities, velocities, ages, and elliptical radii of each stellar population, as listed in Table 4.3. Generally, the older stars are more metal poor and kinematically hotter than the younger stars. It should be stressed however, that the primary variations seen in the data are *radial* velocity and metallicity changes. There is not a substantial spatial change amoung the ages (recall Figure 3.8), no doubt due to the large errors and complications in assigning ages in extragalactic RGB stars. While there is a higher number of stars ≤ 1 Gyr in the bar field of that figure, the more evolved stars show minimal spatial change. This is confirmed unambiguously by a 4-d principal

Table 4.3. Binned Age Metallicity Statistics

Variable	$t < 1$	$1 \leq t \leq 6$	$t > 6$
$\langle [Fe/H] \rangle$ (dex)	-1.21 ± 0.05	-1.23 ± 0.04	-1.55 ± 0.07
$\langle \sigma_{[Fe/H]} \rangle$ (dex)	0.42	0.34	0.22
$\langle v_{hel} \rangle$ (km s^{-1})	-129 ± 1	-130 ± 1	-136 ± 2
$\langle \sigma_v \rangle$ (km s^{-1})	17	16	22
$\langle t \rangle$ (Gyr)	0.2	3.0	15
$\langle r_{ell} \rangle$ (deg.)	0.07	0.09	0.08
$\langle \sigma_r \rangle$ (deg.)	0.05	0.06	0.05
n	30	35	13

Note. — Average values in three age bins, for various parameters of the WLM stellar sample.

component analysis, and a k-means clustering analysis as described below.

While there are essentially four dimensions to the data (spatial, chemical, kinematic and temporal), we need to understand which of these are contributing the most to the correlations and variances, so that analysis and interpretations are not led astray. There are already several clues in previous sections that suggest that many of the variances are being driven primarily by location within the galaxy. However, can it be statistically shown that these are the attributes that capture most of the variance in the data, and not say, the stellar age disparity?

Principal Component Analysis (PCA) offers a method to understand how the behaviour of those attributes influence our analysis. By constructing a 4-D matrix, and

subtracting the mean from the r_{ell}, v_{hel}, [Fe/H], and age columns, it is possible to do a simple decomposition of the data set into new components, in which the coordinate vectors or components are ordered by the amount of variance in the original data that they capture. Table 4.4 shows the results of the first four principal components. The total variance of the dataset is captured by these four highest components, and the first three components account for approximately 88% of the variance. Reduction to a smaller dimensionality is one application of PCA, but here we seek to understand which of the attributes are dominant in creating variance in this 4-D parameter space. By looking at the projection of the attributes onto the principal axes, it is possible to find which one contributes most to the variance captured by a given principal component. As shown in Table 4.5, In each of the four PCA modes, the majority ($\sim 50\%$) of the variance is produced by the first attribute (r_{ell}), with the [Fe/H] and velocity data contributing roughly another 40%. The age attribute is by far the least important in this representation, no doubt due to its small range in parameter space and incomplete distribution.

This idea is reinforced through the method of k-means clustering analysis. This particular method of clustering analysis relies on an algorithm to iteratively decompose and reassign the dataset into n-clusters, which minimize the total variance within each cluster. As the minimum is reached when there is no more reassignment of data within the clusters, it is important to check that the clustering routine is not produc-

ing artificial segregation or variance. For the cases of $n = 2, 3, 4$ clusters, an algorithm was run using IDL routines, multiple times, so as to make sure there was no variation in the result. The fact that the algorithm can start with random cluster centroids but is then able to produce the same cluster results, identifies our dataset as appropriate for this type of analysis. What the results of each value of n showed were that the 4-D clustering is primarily dissociating the dataset into clusters by separating it by one or two attributes. In Figure 4.6, the result of one run of the algorithms for $n = 4$ is shown, expressed as four projections of the WLM dataset. The clusters are arbitrarily given colours and symbols, and clearly the separation that the clustering refinement produced is most visible along the velocity, metallicity and elliptical radii axes. Other representations involving plots of age, showed that the cluster separation becomes unclear. The fact that an iterative clustering algorithm naturally finds the most separable trends in these particular attributes, again suggests that the most dominant correlations in our data involve spatial location, velocity, and metallicity, but not age - essentially confirming what was seen in the PCA results

While, not a perfect diagnostic tool for looking at this type of small number data, these statistical tools, along with trends discussed in the previous section really drive home the point that we are primarily sensitive to metallicity and velocity changes as a function of spatial position. Additional secondary or tertiary correlations between age, or more complicated chemodynamic pairings may exist, but given the asymmetric

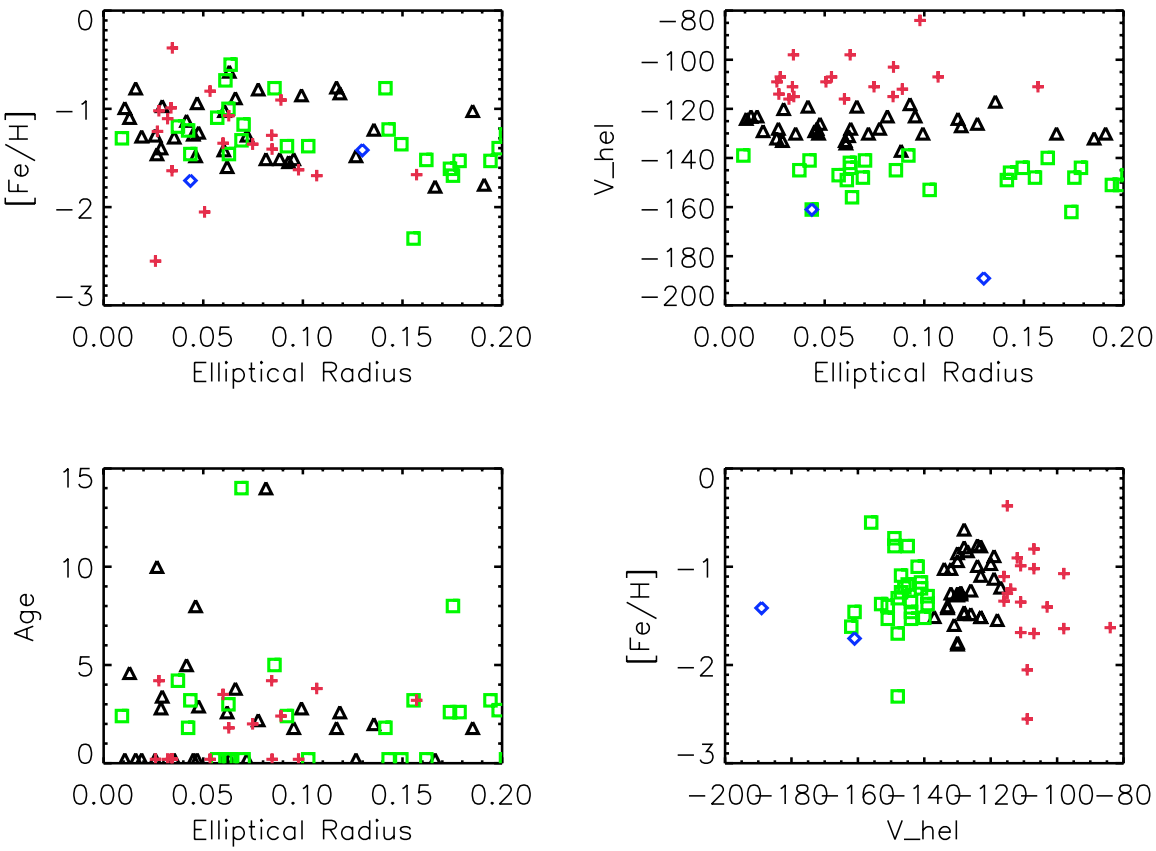

Figure 4.6: One run from the k-means clustering analysis for the full sample of stars in the survey. Shown are four representations of the data that has been iteratively sorted according to Lloyd's algorithm, to search for cluster patterns in the 4-D attribute space of our dataset (see text for details). Evident is the natural cluster separation in velocity and metallicity space, again confirming that most of the variance in the correlations seen are controlled by these strong projections.

age distribution and other complicating factors, we are not as sensitive to them. As such, we stress to the reader that this work primarily answers questions on the global metallicity function of an isolated dwarf irregular galaxy, with additional information on spatial dependencies of its metallicity and kinematics. However full temporal data and a larger sample will be necessary before we can answer more complicated questions

Table 4.4. PCA Results: r_{ell}, v_{hel}, [Fe/H], Age

Mode	Eigenvalue	Percent Variance
1	1.486	37.154
2	1.051	26.283
3	0.982	24.538
4	0.481	12.025

on the chemical and dynamical history of WLM and identify distinct chemodynamic subgroups if they exist.

4.4 Comparison to Gas Dynamics

Of equal interest is the examination of the properties of the stars which do not show the same kinematic traits as the gas (from H I studies). The simplest expectation is that the metal rich stars would have formed from material that is more recently dynamically coupled to the gas, and would have had less time to become kinematically hot. This is borne out by the smaller velocity dispersion amoung the metal rich subsample of the dataset (see §4.2).

In addition to this, we can compare the stellar velocity gradient to that of the H I velocity gradient. Jackson et al. (2004) found an H I velocity gradient consistent with a rotation curve, and Kepley et al. (2007) derived a rotation velocity of ~ 30 km s^{-1} for the gas, with a more steeply varying velocity gradient in the northern approaching

Table 4.5. Attribute Projection onto Principal Modes

Mode	r_{ell}	v_{hel}	[Fe/H]	Age
1	0.542	0.263	0.087	0.108
2	0.549	0.127	0.220	0.104
3	0.438	0.156	0.326	0.081
4	0.371	0.413	0.132	0.084

Note. — Values are projection of the attributes onto the principal component modes, normalized to the eigenvalue of each principal component and expressed as a percentage

side of the galaxy. A direct comparison of the stellar and gas kinematics is shown in Figure 4.7, where the Kepley et al. (2007) H I position-velocity data is overlaid on our stellar velocities. The average velocity separation between the flat central part of our stellar velocity data and the approaching northern section is $\sim$ 15 km s^{-1}. This is statistically significant given the errors of $\pm$6 km s^{-1} per star and error on the mean of $\pm$ 3 km s^{-1}. However the gradient is shallower and only half that of the gas rotation velocity. It is important to note that a small fraction of this may occur naturally due to assymetric drift. An apparent spatial lag is also seen, although the rotation center is consistent with the H I studies. These types of stellar and gas velocity discrepancies may be common in dwarf irregular galaxies, whether isolated or interacting, as witnessed by the massive star kinematics in the Small Magellanic

Cloud reported by Evans and Howarth (2008)

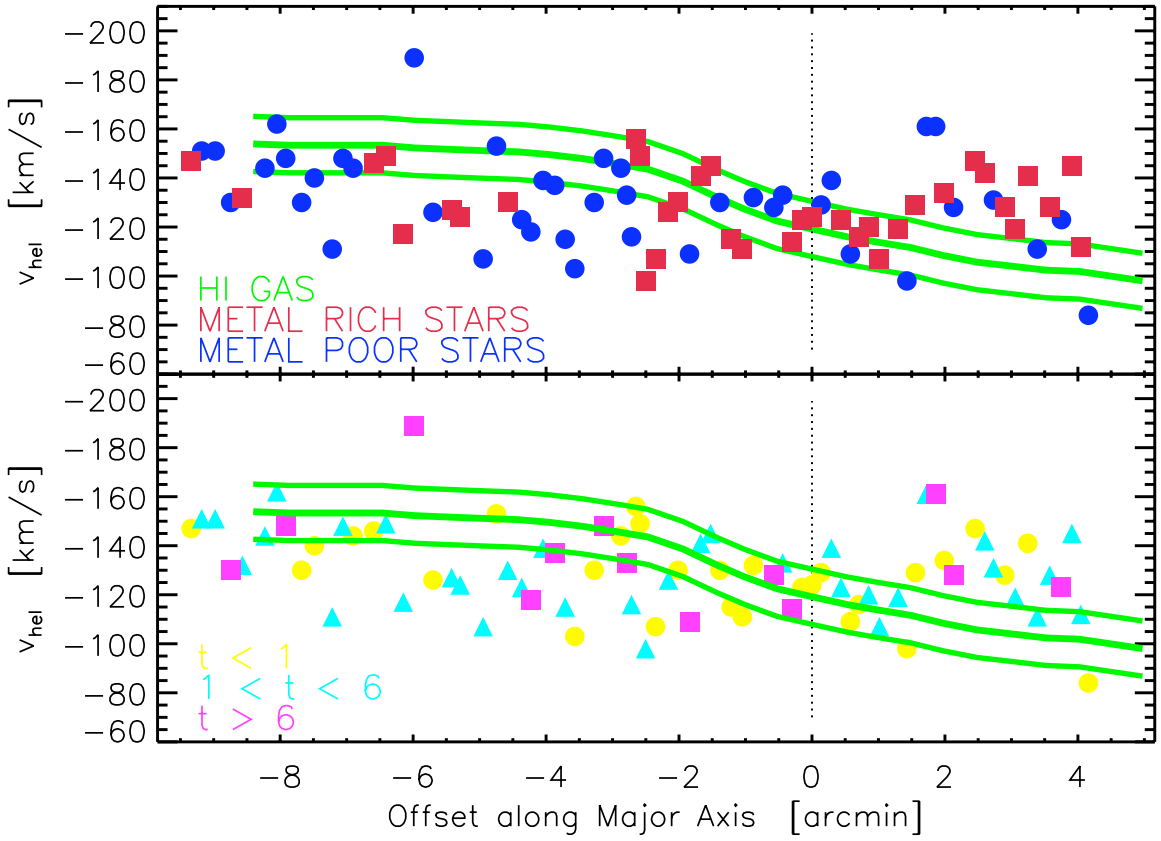

Figure 4.7: (*top panel*) Comparison of the heliocentric stellar velocity data for the metal rich (red), metal poor (blue) WLM subpopulations. Shown in green is the Kepley et al. (2007) H I gas position-velocity data. Neither subpopulation tracks the gas particularly well, and the velocity gradient is only half that seen for the H I data (see text). (*bottom panel*) Similar visualization, but with the WLM stars subdivided into three age bins: $t \leq 1$ Gyr (*yellow circles*), $1 \leq t \leq 6$ Gyr (*cyan triangles*), $t \geq 6$ Gyr (*magenta squares*). Negative offsets along the major axis correspond to the north portion of the galaxy, positive offsets the southern direction.

Clearly the stellar members in this sample are not in the same velocity space as the bulk of the rotating gaseous component of WLM. In the northern part of the galaxy, the stars lag the gas rotation by as much as $\sim$ 35 km s^{-1}. At the southern most part of our fields, the stars show a velocity offset of roughly the same magnitude, but opposite sign. To fully explain the complex velocity decoupling seen between the stellar and gaseous components of WLM will take a larger sample, but Figure 4.7 nicely illustrates the lack of coherent motion.

To quantify the difference in velocity of the stars from the gaseous components, a parameter $\Delta V_{(star-gas)}$ was calculated as follows. For each star in Figure 4.7, an offset in velocity was found by subtracting the stars velocity from the velocity of the gas at that declination in WLM (according to the Kepley et al. (2007) position-velocity data). This was done to search for subsamples of stars that track the gas velocity the closest. If the H I gas of WLM forms a thin rotating plane, we might expect that the youngest stars in our sample track this better, than say, the oldest stars.

There are a couple notes on this analysis. First of all, the position-velocity curve from Kepley et al. (2007) was taken from a band of gas down the major-axis of WLM. Whereas our stars cover a range in positions off the major axis as well. These stars that lay off the major axis will naturally lag the gas, due to the shape of the H I isovelocity contours in the far north of WLM. However by looking at the isovelocity contours for WLM in the Kepley et al. (2007) study, it is possible to quntify the

amount of this lag. For declinations where this effect is the greatest, the offset is estimated to be $\lesssim 10$ km s^{-1}, contributing at most 25% to the observed $\Delta V_{(star-gas)}$ value for that region. However, for the vast majority of our sample, differential rotation has a negligible effect *and* there is no correlation between distance from the major axis and $\Delta V_{(star-gas)}$ when we plot those indicators. The inclination of WLM, and possibility of a spheroidal stellar configuration also adds uncertainty to the true spatial proximity of these components of WLM - as the planar coordinates used cannot account for the three dimensional geometry of the stars and gas. Regardless, with careful accounting of these biases, this $\Delta V_{(star-gas)}$ provides a useful first order comparsion of the stellar and gas velocities.

In Figure 4.8, $\Delta V_{(star-gas)}$ is plotted against v_{hel}, age, and metallicity. While there is some substructure in these representations, no clear trends emerge. This suggests that the stellar occupation of the H I velocity space is essentially random - implying that all stellar age bins/populations have been dynamically excited from the H I bulk motion. This would be consistent with the stellar population of WLM laying in a thick disk and/or spheroidal configuration. Even the youngest stars show a range in $\Delta V_{(star-gas)}$, thus either the gas and stars were never coupled (e.g., if the gas was recently accreted) or the mechanism responsible for dynamically decoupling the stellar velocities from the gas must have been present within the last few Gyr.

A bar in a past epoch of WLM's history, may provide a natural explanation to the

lack of coherent chemistry and ages amoungst the stars that track the gas velocities the closest (recall Figure 4.8). Bars will dynamically stir a stellar population in a low mass galaxy such as WLM, and this offers an explanation for the large velocity dispersions and velocity offsets in our sample when compared to the gas. Olsen and Massey (2007) noted tidal heating may be responsible for a dynamically hot component in the stellar disk of the LMC. However, given the isolation of WLM, a past bar may be a more feasible explanation for the dynamically hot component of WLM's stellar body.

The standard deviation of our $\Delta V_{star-gas}$ value is approximately $\sigma_{\Delta V} \sim 24$ km s^{-1}. This can be thought of as the dispersion of the deviation between the young (gaseous) and old (stellar) populations. This dispersion in the velocity offset is larger than both the H I internal dispersion ($\sigma_{HI} \sim 5$ km s^{-1}; Kepley et al. 2007), and the dispersion of the youngest stars in this sample ($\sigma_{t<1} \sim 17$ km s^{-1}), but approaches the dispersion of our oldest stars ($\sigma_{t>6} \sim 22$ km s^{-1}). This is perhaps analogous to results for the LMC in the work of Olsen and Massey (2007), which showed a similar trend in that the dispersion in the difference in velocities for the young and old population, approached the internal dispersion of the oldest population. They mentioned that this implies a dynamical mixing over time to a systemic dispersion, which could be seen as evidence for tidal heating of the stellar disk in the LMC. Here, the resonances of a bar would be the responsible mechanism, rather than the potential of the MW,

but the similarities are interesting.

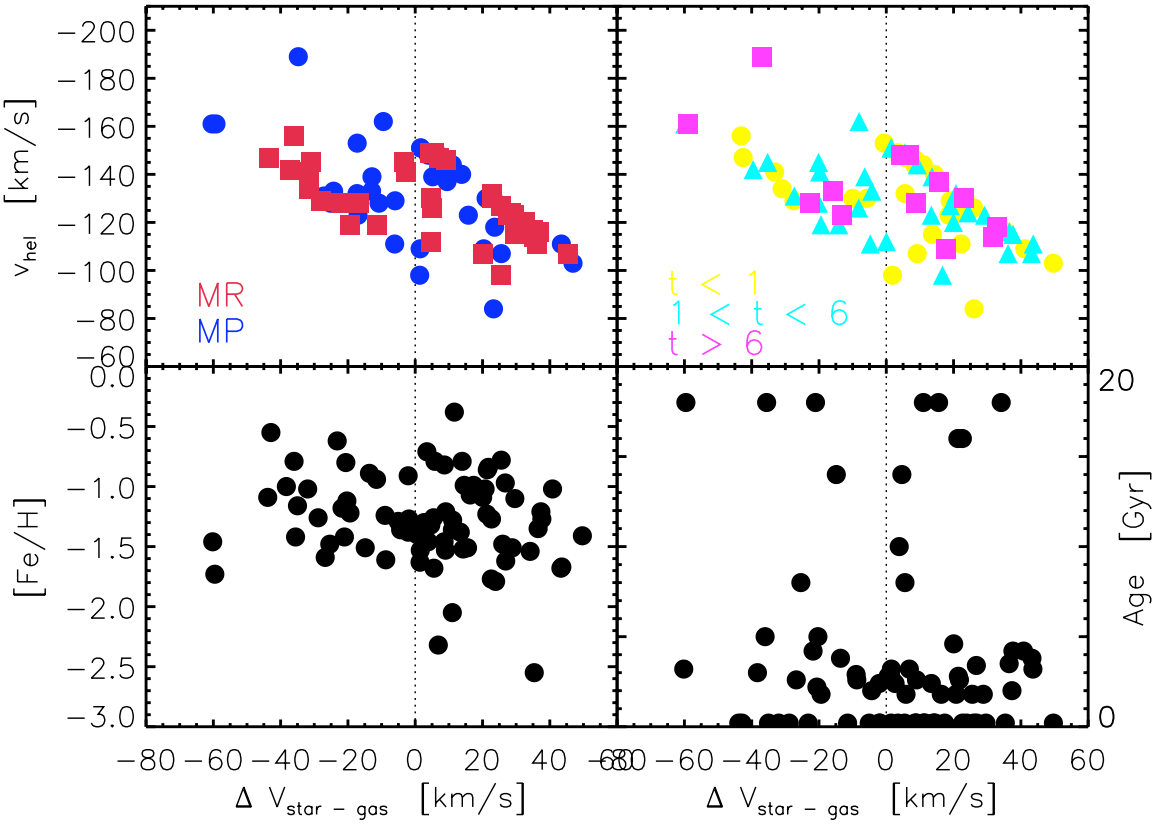

Figure 4.8: Shown is the stellar to gas velocity offset ($\Delta V_{(star-gas)}$; see text) for all stars in the sample, compared against various parameters. Upper panels show the $\Delta V_{(star-gas)}$ values versus v_{hel} for metallicity bins, and age bins (symbols are the same as in Figure 4.7). (*bottom panels*) $\Delta V_{(star-gas)}$ plotted versus [Fe/H] and age. No clear trend exists between the star-gas velocity offset and the metallicity or age values, suggesting the stellar occupation of the H I velocity space is essentially random.

Comparison of stellar velocities with the small scale H I features is also possible with our accurate velocities and positions. The two most recent neutral hydrogen studies of WLM both identify a centrally evacuated region in the disk. Kepley et al. (2007) suggested that this low density gas region, when combined with Hα indicators, was the result of concentrated SF, and subsequent supernovae explosions pushing the gas outward to some radius. Kepley et al. (2007) identify this as a ring or "hook" feature; Jackson et al. (2004) noted that the features were consistent with either a central bar *or* a massive blowout region.

Figure 4.9 shows one result of binning the stars in r_{ell} space, and calculating the σ_v profile for various subpopulations. The young and metal rich, old and metal poor populations show similar trends for this binning. The bottom panel shows a binning in metallicity space, illustrating a slight decline in σ_v with increasing [Fe/H]. These visualizations are useful in comparing the stellar dynamics to localized small scale H I motion and structure as introduced in the previous paragraph. We find that the extent of the blowout ring or bar identified by Kepley et al. (2007), corresponds to the peak velocity dispersion for our metal rich (and youngest) stars as seen in Figure 4.10.

If this turbulent small H I structure is indeed due to an expanding shell, Kepley et al. (2007) place an upper limit on the age of the ring at 128 Myr. Our metal rich stars that have a σ_v peak at this location are also young, but most likely older than

0.1 Gyr (we cannot derive ages below 1.6 Gyr). Thus, if our metal rich (and youngest) stars responded dynamically to this feature, and showed increased velocity dispersion at this location, it must be older than estimated by Kepley et al. (2007). Older stars should not respond to a turbulent shock front that did not exist in this region at the time of their birth, so a supernova blowout in this area would not be responsible for the velocity dispersion peak amongst our metal rich stars.

Alternatively, the feature could be caused by something else (perhaps a resonance) and the gas is only sampling the current effect, whereas the stars in our sample suggest that its impact has been around a lot longer. Dynamical stirring or resonances from a bar could operate over longer timescales, even several Gyr. This suggests that the underlying physical mechanism for the σ_v peak at the H I feature, may be a resonance associate with a past bar in WLM. Jackson et al. (2004) suggested this possibility to explain the central deficit and ring, and while Kepley et al. (2007) favour a central expanding shell feature, they note that they cannot rule out the possibility of a bar; in that scenario, an excess of gas would accumulate near the ends of the bar radius. Interestingly, Kepley et al. (2007) estimate that as much as 20% of the total mass of WLM may be contained within the ring/hook structure, consistent with a bar scenario as well. Clearly, larger numbers are needed to confirm the velocity dispersion peak at the location of the Kepley et al. (2007) ring feature, and also to further accurate comparison between the stellar and H I velocities. However the thick stellar disk

suggested by our velocity offsets, as well as the velocity dispersion peak near the central ring feature in the H I, both hint at there being a bar in the recent history of WLM. Confirming these two findings will be one of the primary goals of future stellar chemodynamic studies of WLM.

A similar correlation may exist between the metal *poor* (and oldest) subsamples and declination where the gas rotation changes from solid body to differential rotation. This radius is found from the dynamical mass estimates and rotation curve analysis done by both Kepley et al. (2007) and Jackson et al. (2004). Without additional information about the mass profile of WLM, it is impossible to say if this stellar dispersion peak is correlated by chance, or perhaps can be related to a larger picture of the dynamical history of WLM.

The ratio of rotation velocity to velocity dispersion ($\frac{v_{rot}}{\sigma_v}$) can provide information on the amount that a galaxy's structure is rotationally supported. In Table 4.6, this ratio is compared for the full sample of RGB stars, and various subpopulations. The stellar velocity ratio for the full sample is lower than that derived for the gas kinematics in Mateo (1998), although the gas velocity dispersion and the central density were assumed quantities. The stellar rotational velocities were estimated by linearly fitting the heliocentric velocities versus elliptical radii. As expected, the metal poor, old, and "halo-like" subdivisions produce lower relative $\frac{v_{rot}}{\sigma_v}$ ratios than the other splits. These results suggest that the older stellar population in WLM

Table 4.6. Subpopulation $\frac{v_{rot}}{\sigma_v}$ Ratios

Component	v_{rot}	σ_v	$\frac{v_{rot}}{\sigma_v}$
Full Sample	20.78	17.53	1.19
Metal Rich	20.61	14.29	1.44
Metal Poor	19.64	19.91	0.99
$t < 1$ Gyr	22.55	17.31	1.30
$1 \leq t \leq 6$ Gyr	17.52	16.14	1.09
$t > 6$ Gyr	9.90	15.20	0.65
HI-like velocities ("disk")	40.50	13.50	3.00
non-HI-like velocities ("halo")	22.86	18.67	1.23

Note. — The final two rows separate the sample based on those stars that fall in the same position-velocity space as the Kepley et al. (2007) H I velocity data.

is more pressure supported, while the younger stellar population (and gas) is more rotationally supported. While *all* of our stars lay off the plane occupied by the gas in position-velocity space, and appear dynamically excited and decoupled from the gas motion - we see a range of $\frac{v_{rot}}{\sigma_v}$ for the stellar subpopulations *within* that thick disk of stars itself.

Thus the stellar velocities, when compared with the gas motions, suggested an excited thick disk or spheroidal configurations for the stars. Given the isolation of WLM, dynamical excitation of the stellar component is perhaps better explained by a long lived bar in a past epoch of WLM's history. The velocity dispersion profiles show

a correlation with the central ring feature from H I studies, which may also be related to the effects and presence of a past bar. While all of these results are intriguing, we stress that this work is limited by a very small statistical sample. A larger sample of stars is necessary to examine this and other results, and ultimately test the conditions of the isolated dwarf galaxies from the earliest epochs of star formation to the present.

4.5 Future Prospects

As detailed studies of the old populations in distant dIrr galaxies are science drivers for many of the large next generation telescopes, it would be useful to derive more sophisticated target preselection of RGB stars. Simple unbiased colour and magnitude preselection of stars near the tip of the RGB may fail to completely sample a dwarf irregular galaxy with complicated star formation and composite populations. Therefore multiwavelength information should be considered essential to rule out AGB contaminants, or weak CH stars that may contaminate the sample - as they are not appropriate for the CaT method. Spitzer colours or other infrared data may work at accurately weeding out *some* contaminating members near the RGB tip (see e.g. Jackson et al. 2007).

In addition to minimizing contamination, is it possible to design specific spectrophotometric studies to sample the *most evolved* RGB stars in local group dwarfs? Rather than accessing the old population in these galaxies through brute force, large

number spectroscopic surveys (which are observationally expensive), it would be invaluable to be able to observe only the stars which are the oldest tracers of the galaxies history. This of course is rather difficult, but many options for this have been used in our own Milky Way galaxy. Objective prism surveys formed the basis for selecting the most metal poor stars in the Hamburg/ESO survey (Beers and Christlieb, 2005), however these are insensitive and impractical for the crowded stellar fields in extragalactic galaxies. Stromgren and Washington photometric systems offer one possibility for preselecting the most evolved RGB stars in composite dwarf galaxy populations. The narrow band photometric indices created in both systems allow for separation by luminosity class and metallicity. Both systems have been successful for nearer dwarf galaxies than WLM (Hughes et al. 2008), but are limited by the narrowness of the filter bands when applied to more distant galaxies. The largest telescope that currently provides Stromgren and Washington filters is the 3.5m ARC telescope at the Apache Point Observatory. Unfortunately our test run of observations on WLM with this system was clouded over, but future applications of this photometric preselection to more distant populations will be possible with this (or hopefully larger) telescopes.

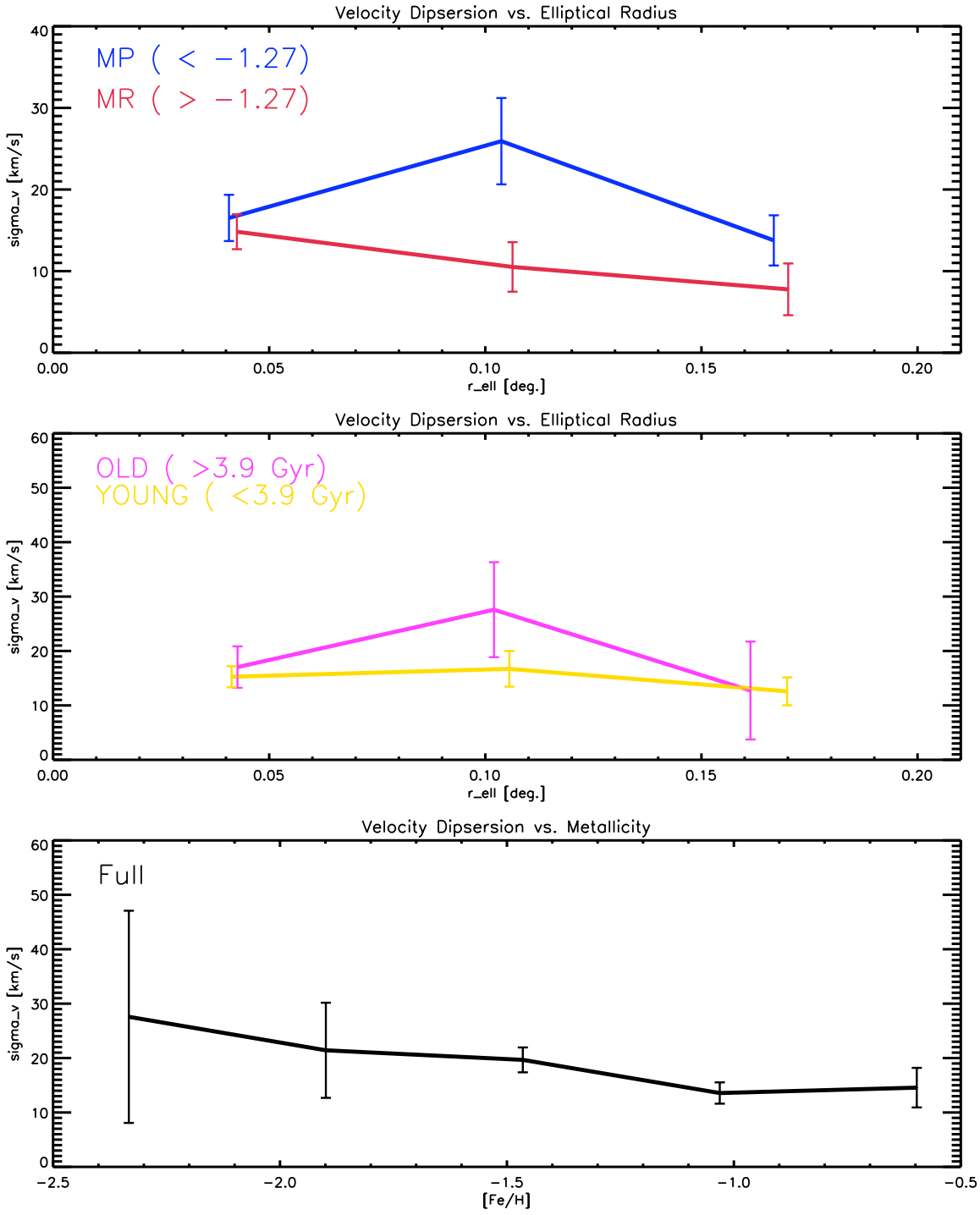

Figure 4.9: Values of σ_v for various binnings in elliptical radii, and metallicity space. The metal poor, and old divisions display similar velocity dispersion trends with radii, as do the paring of young and metal rich stars.

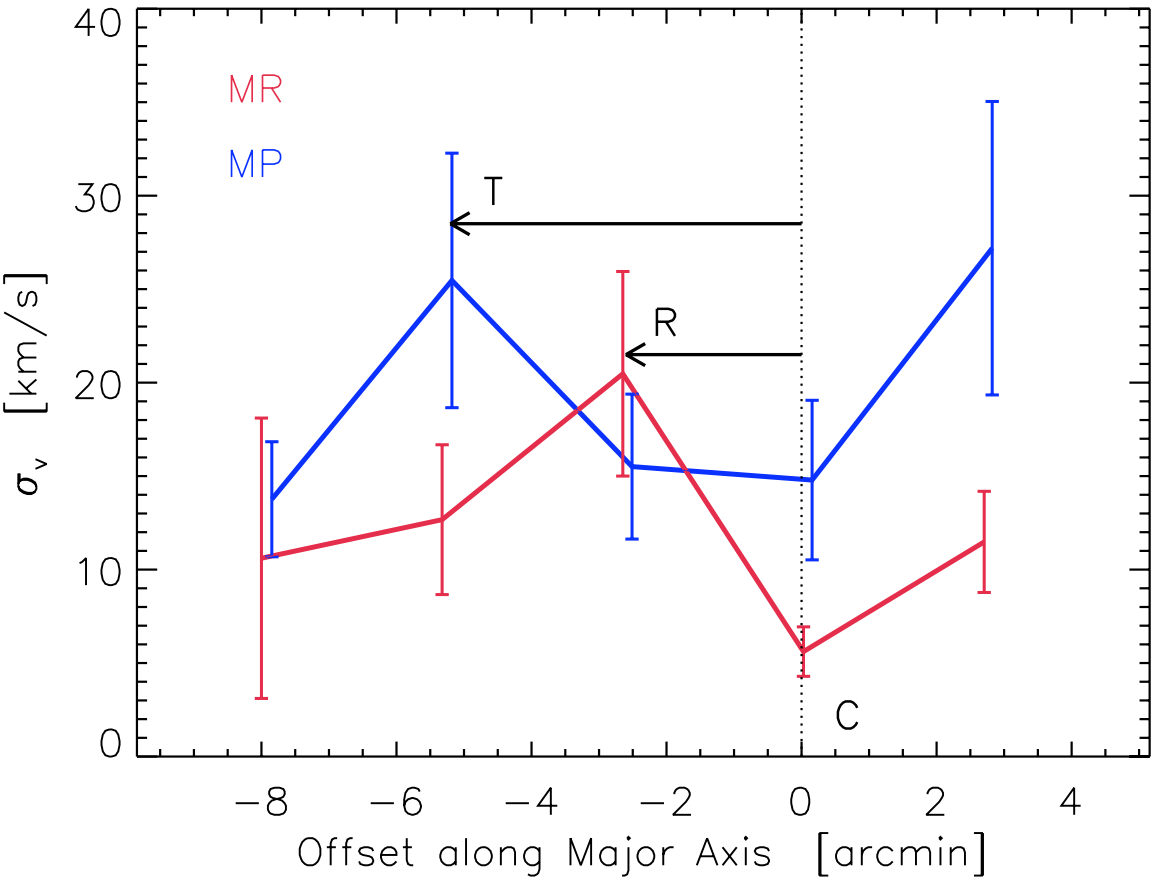

Figure 4.10: Binned velocity dispersion versus offset along the major axis, for the metal rich and metal poor stellar subpopulations. Overlaid are arrows indicating the locations of interesting gas features, and their relative distance from the centre (C; defined by the H I rotation) of WLM. Shown are the radii where gas rotation transitions from solid body to differential rotation (T), and the extent of the central blowout or bar region (R). The corresponding velocity dispersion maxima and minima are discussed in the text.

Chapter 5

Conclusions

We have presented the first detailed analysis of the Ca II triplet spectra of 78 individual RGB stars in the isolated dwarf irregular galaxy WLM. Medium resolution spectra taken with the FORS2 spectrograph at the VLT in two fields in this galaxy (a central bar region, and a northern field) were coadded to improve the SNR ≥ 20. This is the first analysis of such faint RGB stars for *both* velocity and metallicity measurements, and therefore we have been careful in our data reduction techniques and error propagation calculations. The equivalent widths were converted into metallicities for each star using the calibration from Cole et al. (2004) with final errors $\sim \pm 0.25$ dex per star. The heliocentric velocities were determined to within ± 6 km s^{-1} (random error). Relative ages were derived from theoretical stellar evolution models, however differential extinction and selection effects limit the completeness of our age distribu-

tion.

The north field and bar field metallicity distributions have mean metallicities and dispersions of [Fe/H]= -1.45 ± 0.04, $\sigma = 0.33$ from 34 stars, and [Fe/H]= -1.14 ± 0.04, $\sigma = 0.39$ from 44 stars, respectively. Both metallicity distributions are narrowly constrained with a range of approximately Δ[Fe/H]$\simeq$ 1.0. The stars in our sample show radial metallicity, and velocity gradients, but interestingly the stellar rotation velocity is only approximately half that of the gas. The stellar velocities appear to be kinematically decoupled and in a thicker disk than the gas. Detailed comparisons with the H I gas, along with the isolation of WLM, suggest that the gas and stars were never coupled (e.g., recent H I infall) or that the stellar dynamics have been affected by resonances associated with a past bar.

WLM shows signatures of a metal poor population that is spatially and temporally distinct, and kinematically hotter than the young population at all radii - perhaps indicative of an extended halo. The velocities of the older stars suggest that this evolved stellar population in WLM is pressure supported, as opposed to the younger stars and gas disk which appear more rotationally supported. This latter result rests on a very small number of old RGB stars (13 with t $\geq$ 6 Gyr), but could have significant consequences for constraining theories of the structure and dynamics of dwarf galaxies in the early Universe. A larger sample and survey size is necessary to confirm these results and further characterize the stellar populations in WLM.

Bibliography

H. D. Ables and P. G. Ables. B, V photometry of the WLM galaxy. *ApJS*, 34: 245–258, June 1977.

T. E. Armandroff and G. S. Da Costa. Metallicities for old stellar systems from Ca II triplet strengths in member giants. *AJ*, 101:1329–1337, April 1991. doi: 10.1086/115769.

D. G. Barnes and W. J. G. de Blok. The neutral hydrogen environments of the nearby galaxies WLM, NGC 1313 and Sextans A. *MNRAS*, 351:333–338, June 2004. doi: 10.1111/j.1365-2966.2004.07790.x.

G. Battaglia, E. Tolstoy, A. Helmi, M. J. Irwin, B. Letarte, P. Jablonka, V. Hill, K. A. Venn, M. D. Shetrone, N. Arimoto, F. Primas, A. Kaufer, P. Francois, T. Szeifert, T. Abel, and K. Sadakane. The DART imaging and CaT survey of the Fornax dwarf spheroidal galaxy. *A&A*, 459:423–440, November 2006. doi: 10.1051/0004-6361:20065720.

G. Battaglia, M. Irwin, E. Tolstoy, V. Hill, A. Helmi, B. Letarte, and P. Jablonka. Analysis and calibration of CaII triplet spectroscopy of Red Giant Branch stars from VLT/FLAMES observations. *ArXiv e-prints*, 710, October 2007.

P. Battinelli and S. Demers. Carbon star survey of Local Group galaxies. X. Wolf-Lundmark-Melotte a galaxy with an extreme C/M ratio. *A&A*, 416:111–118, March 2004. doi: 10.1051/0004-6361:20034557.

T. C. Beers and N. Christlieb. The Discovery and Analysis of Very Metal-Poor Stars in the Galaxy. *ARA&A*, 43:531–580, September 2005.

T. L. Bosler, T. A. Smecker-Hane, and P. B. Stetson. The chemical abundances of the stellar populations in the Leo I and II dSph galaxies. *MNRAS*, 378:318–338, June 2007. doi: 10.1111/j.1365-2966.2007.11792.x.

F. Bresolin, G. Pietrzyński, M. A. Urbaneja, W. Gieren, R.-P. Kudritzki, and K. A. Venn. The Araucaria Project: VLT Spectra of Blue Supergiants in WLM- Classification and First Abundances. *ApJ*, 648:1007–1019, September 2006. doi: 10.1086/506200.

C. Brook, S. Richard, D. Kawata, H. Martel, and B. K. Gibson. Two Disk Components from a Gas-Rich Disk-Disk Merger. *ApJ*, 658:60–64, March 2007. doi: 10.1086/511056.

R. Carrera, C. Gallart, E. Hardy, A. Aparicio, and R. Zinn. The Chemical Enrichment History of the Large Magellanic Cloud. *ArXiv e-prints*, 710, October 2007a.

R. Carrera, C. Gallart, E. Pancino, and R. Zinn. The Infrared Ca II Triplet as Metallicity Indicator. *AJ*, 134:1298–1314, September 2007b. doi: 10.1086/520803.

E. Carretta and R. G. Gratton. Abundances for globular cluster giants. I. Homogeneous metallicities for 24 clusters. *A&AS*, 121:95–112, January 1997.

R. Cayrel. Data Analysis. In G. Cayrel de Strobel and M. Spite, editors, *The Impact of Very High S/N Spectroscopy on Stellar Physics*, volume 132 of *IAU Symposium*, pages 345–+, 1988.

A. J. Cenarro, N. Cardiel, J. Gorgas, R. F. Peletier, A. Vazdekis, and F. Prada. Empirical calibration of the near-infrared Ca ii triplet - I. The stellar library and index definition. *MNRAS*, 326:959–980, September 2001. doi: 10.1046/j.1365-8711.2001.04688.x.

A. J. Cenarro, J. Gorgas, N. Cardiel, A. Vazdekis, and R. F. Peletier. Empirical calibration of the near-infrared Ca II triplet - III. Fitting functions. *MNRAS*, 329: 863–876, February 2002. doi: 10.1046/j.1365-8711.2002.05029.x.

A. A. Cole, T. A. Smecker-Hane, E. Tolstoy, T. L. Bosler, and J. S. Gallagher. The

effects of age on red giant metallicities derived from the near-infrared CaII triplet. *MNRAS*, 347:367–379, January 2004. doi: 10.1111/j.1365-2966.2004.07223.x.

A. A. Cole, E. Tolstoy, J. S. Gallagher, III, and T. A. Smecker-Hane. Spectroscopy of Red Giants in the Large Magellanic Cloud Bar: Abundances, Kinematics, and the Age-Metallicity Relation. *AJ*, 129:1465–1482, March 2005. doi: 10.1086/428007.

A. A. Cole, A. J. Grocholski, D. Geisler, A. Sarajedini, V. V. Smith, and E. Tolstoy. In J. Th. van Loon and J. M. Oliveira, editors, *The Magellanic System: Star, Gas and Galaxies*, volume 256 of *IAU Symposium*, 2008.

F. De Angeli, G. Piotto, S. Cassisi, G. Busso, A. Recio-Blanco, M. Salaris, A. Aparicio, and A. Rosenberg. Galactic Globular Cluster Relative Ages. *AJ*, 130:116–125, July 2005. doi: 10.1086/430723.

J. F. Dean, P. R. Warren, and A. W. J. Cousins. Reddenings of Cepheids using BVI photometry. *MNRAS*, 183:569–583, June 1978.

S. Demers, P. Battinelli, and E. Artigau. Carbon stars in the outer spheroid of NGC 6822. *A&A*, 456:905–910, September 2006. doi: 10.1051/0004-6361:20065507.

A. E. Dolphin. Hubble Space Telescope Studies of the WLM Galaxy. II. The Star Formation History from Field Stars. *ApJ*, 531:804–812, March 2000. doi: 10.1086/308512.

C. J. Evans and I. D. Howarth. Kinematics of massive stars in the Small Magellanic Cloud. *MNRAS*, 386:826–834, May 2008. doi: 10.1111/j.1365-2966.2008.13012.x.

L. Gallouet, N. Heidmann, and F. Dampierre. Optical positions of bright galaxies. III. *A&AS*, 19:1–19, 1975.

W. Gieren, G. Pietrzyński, O. Szewczyk, I. Soszyński, F. Bresolin, R.-P. Kudritzki, M. A. Urbaneja, J. Storm, and D. Minniti. The Araucaria Project: The Distance to the Local Group Galaxy WLM from Near-Infrared Photometry of Cepheid Variables. *ApJ*, 683:611–619, August 2008. doi: 10.1086/589994.

N. Y. Gnedin and A. V. Kravtsov. Fossils of Reionization in the Local Group. *ApJ*, 645:1054–1061, July 2006. doi: 10.1086/504404.

A. J. Grocholski, A. A. Cole, A. Sarajedini, D. Geisler, and V. V. Smith. Ca II Triplet Spectroscopy of Large Magellanic Cloud Red Giants. I. Abundances and Velocities for a Sample of Populous Clusters. *AJ*, 132:1630–1644, October 2006. doi: 10.1086/507303.

W. E. Harris. A Catalog of Parameters for Globular Clusters in the Milky Way. *AJ*, 112:1487–+, October 1996. doi: 10.1086/118116.

A. Helmi, M. J. Irwin, E. Tolstoy, G. Battaglia, V. Hill, P. Jablonka, K. Venn, M. Shetrone, B. Letarte, N. Arimoto, T. Abel, P. Francois, A. Kaufer, F. Primas,

K. Sadakane, and T. Szeifert. A New View of the Dwarf Spheroidal Satellites of the Milky Way from VLT FLAMES: Where Are the Very Metal-poor Stars? *ApJ*, 651:L121–L124, November 2006. doi: 10.1086/509784.

P. Hodge and B. W. Miller. H II Regions in Four Galaxies in and near the Local Group. *ApJ*, 451:176–+, September 1995. doi: 10.1086/176209.

P. W. Hodge, A. E. Dolphin, T. R. Smith, and M. Mateo. Hubble Space TelescopeStudies of the WLM Galaxy. I. The Age and Metallicity of the Globular Cluster. *ApJ*, 521:577–581, August 1999. doi: 10.1086/307595.

W. K. Huchtmeier, J. H. Seiradakis, and J. Materne. The neutral hydrogen distribution of irregular galaxies. *A&A*, 102:134–141, September 1981.

D. C. Jackson, E. D. Skillman, J. M. Cannon, and S. Côté. H I Observations of the Local Group Dwarf WLM. *AJ*, 128:1219–1227, September 2004. doi: 10.1086/423292.

D. C. Jackson, J. M. Cannon, E. D. Skillman, H. Lee, R. D. Gehrz, C. E. Woodward, and E. Polomski. Hot Dust and Polycyclic Aromatic Hydrocarbon Emission at Low Metallicity: A Spitzer Survey of Local Group and Other Nearby Dwarf Galaxies. *ApJ*, 646:192–204, July 2006. doi: 10.1086/504707.

D. C. Jackson, E. D. Skillman, R. D. Gehrz, E. Polomski, and C. E. Woodward. A

Spitzer IRAC Census of the Asymptotic Giant Branch Populations in Local Group Dwarfs. I. WLM. *ApJ*, 656:818–830, February 2007. doi: 10.1086/510354.

U. G. Jorgensen, M. Carlsson, and H. R. Johnson. The Calcium Infrared Triplet Lines in Stellar Spectra. *A&A*, 254:258–+, February 1992.

T. Kaufmann, L. Mayer, J. Wadsley, J. Stadel, and B. Moore. Angular momentum transport and disc morphology in smoothed particle hydrodynamics simulations of galaxy formation. *MNRAS*, 375:53–67, February 2007. doi: 10.1111/j.1365-2966.2006.11314.x.

A. A. Kepley, E. M. Wilcots, D. A. Hunter, and T. Nordgren. A High-Resolution Study of the H I Content of Local Group Dwarf Irregular Galaxy WLM. *AJ*, 133:2242–2257, May 2007. doi: 10.1086/513716.

A. Koch, E. K. Grebel, R. F. G. Wyse, J. T. Kleyna, M. I. Wilkinson, D. R. Harbeck, G. F. Gilmore, and N. W. Evans. Complexity on Small Scales: The Metallicity Distribution of the Carina Dwarf Spheroidal Galaxy. *AJ*, 131:895–911, February 2006. doi: 10.1086/499490.

H. Lee, E. D. Skillman, and K. A. Venn. Investigating the Possible Anomaly between Nebular and Stellar Oxygen Abundances in the Dwarf Irregular Galaxy WLM. *ApJ*, 620:223–237, February 2005. doi: 10.1086/427019.

P. Madau, A. Ferrara, and M. J. Rees. Early Metal Enrichment of the Intergalactic Medium by Pregalactic Outflows. *ApJ*, 555:92–105, July 2001. doi: 10.1086/321474.

M. L. Mateo. Dwarf Galaxies of the Local Group. *ARA&A*, 36:435–506, 1998. doi: 10.1146/annurev.astro.36.1.435.

L. Mayer, C. Mastropietro, J. Wadsley, J. Stadel, and B. Moore. Simultaneous ram pressure and tidal stripping; how dwarf spheroidals lost their gas. *MNRAS*, 369: 1021–1038, July 2006. doi: 10.1111/j.1365-2966.2006.10403.x.

A. W. McConnachie, M. J. Irwin, A. M. N. Ferguson, R. A. Ibata, G. F. Lewis, and N. Tanvir. Distances and metallicities for 17 Local Group galaxies. *MNRAS*, 356: 979–997, January 2005. doi: 10.1111/j.1365-2966.2004.08514.x.

A. W. McConnachie, K. A. Venn, M. J. Irwin, L. M. Young, and J. J. Geehan. Ram Pressure Stripping of an Isolated Local Group Dwarf Galaxy: Evidence for an Intragroup Medium. *ApJ*, 671:L33–L36, December 2007. doi: 10.1086/524887.

D. Minniti and A. A. Zijlstra. Stellar Populations of the Dwarf Irregular Galaxy WLM. *AJ*, 114:147–160, July 1997. doi: 10.1086/118461.

B. Moore, S. Ghigna, F. Governato, G. Lake, T. Quinn, J. Stadel, and P. Tozzi. Dark Matter Substructure within Galactic Halos. *ApJ*, 524:L19–L22, October 1999. doi: 10.1086/312287.

J. F. Navarro, C. S. Frenk, and S. D. M. White. A Universal Density Profile from Hierarchical Clustering. *ApJ*, 490:493–+, December 1997. doi: 10.1086/304888.

K. A. G. Olsen and P. Massey. Evidence for Tidal Effects in the Stellar Dynamics of the Large Magellanic Cloud. *ApJ*, 656:L61–L64, February 2007. doi: 10.1086/512484.

D. E. Osterbrock and A. Martel. Sky spectra at a light-polluted site and the use of atomic and OH sky emission lines for wavelength calibration. *PASP*, 104:76–82, January 1992.

F. Pont, R. Zinn, C. Gallart, E. Hardy, and R. Winnick. The Chemical Enrichment History of the Fornax Dwarf Spheroidal Galaxy from the Infrared Calcium Triplet. *AJ*, 127:840–860, February 2004. doi: 10.1086/380608.

B. J. Pritzl, K. A. Venn, and M. Irwin. A Comparison of Elemental Abundance Ratios in Globular Clusters, Field Stars, and Dwarf Spheroidal Galaxies. *AJ*, 130:2140–2165, November 2005. doi: 10.1086/432911.

M. Rejkuba, D. Minniti, M. D. Gregg, A. A. Zijlstra, M. V. Alonso, and P. Goudfrooij. Deep Hubble Space Telescope STIS Color-Magnitude Diagrams of the Dwarf Irregular Galaxy WLM: Detection of the Horizontal Branch. *AJ*, 120:801–809, August 2000. doi: 10.1086/301501.

M. Ricotti and N. Y. Gnedin. Formation Histories of Dwarf Galaxies in the Local Group. *ApJ*, 629:259–267, August 2005. doi: 10.1086/431415.

G. A. Rutledge, J. E. Hesser, and P. B. Stetson. Galactic Globular Cluster Metallicity Scale from the Ca II Triplet II. Rankings, Comparisons, and Puzzles. *PASP*, 109: 907–919, August 1997.

D. J. Schlegel, D. P. Finkbeiner, and M. Davis. Maps of Dust Infrared Emission for Use in Estimation of Reddening and Cosmic Microwave Background Radiation Foregrounds. *ApJ*, 500:525–+, June 1998. doi: 10.1086/305772.

T. Schoerck, N. Christlieb, J. G. Cohen, T. C. Beers, S. Shectman, I. Thompson, A. McWilliam, M. S. Bessell, J. E. Norris, J. Melendez, S. Solange Ramirez, D. Haynes, P. Cass, M. Hartley, K. Russell, F. Watson, F. . Zickgraf, B. Behnke, C. Fechner, B. Fuhrmeister, P. S. Barklem, B. Edvardsson, A. Frebel, L. Wisotzki, and D. Reimers. The stellar content of the Hamburg/ESO survey. V. The metallicity distribution function of the Galactic halo. *ArXiv e-prints*, September 2008.

E. D. Skillman, R. Terlevich, and J. Melnick. Abundances in southern Local Group dwarf irregular galaxies. *MNRAS*, 240:563–572, October 1989.

P. B. Stetson. The center of the core-cusp globular cluster M15: CFHT and HST Observations, ALLFRAME reductions. *PASP*, 106:250–280, March 1994.

E. Tolstoy. UVES Abundances of Stars in Nearby Galaxies: How Good Are Theoretical Isochrones? In G. Piotto, G. Meylan, S. G. Djorgovski, and M. Riello, editors, *New Horizons in Globular Cluster Astronomy*, volume 296 of *Astronomical Society of the Pacific Conference Series*, pages 234–+, 2003.

E. Tolstoy, M. J. Irwin, A. A. Cole, L. Pasquini, R. Gilmozzi, and J. S. Gallagher. Using the Ca ii triplet to trace abundance variations in individual red giant branch stars in three nearby galaxies. *MNRAS*, 327:918–938, November 2001. doi: 10.1046/j.1365-8711.2001.04785.x.

E. Tolstoy, K. A. Venn, M. Shetrone, F. Primas, V. Hill, A. Kaufer, and T. Szeifert. VLT/UVES Abundances in Four Nearby Dwarf Spheroidal Galaxies. II. Implications for Understanding Galaxy Evolution. *AJ*, 125:707–726, February 2003. doi: 10.1086/345967.

E. Tolstoy, M. J. Irwin, A. Helmi, G. Battaglia, P. Jablonka, V. Hill, K. A. Venn, M. D. Shetrone, B. Letarte, A. A. Cole, F. Primas, P. Francois, N. Arimoto, K. Sadakane, A. Kaufer, T. Szeifert, and T. Abel. Two Distinct Ancient Components in the Sculptor Dwarf Spheroidal Galaxy: First Results from the Dwarf Abundances and Radial Velocities Team. *ApJ*, 617:L119–L122, December 2004. doi: 10.1086/427388.

M. A. Urbaneja, R. . Kudritzki, F. Bresolin, N. Przybilla, W. Gieren, and G. Pietrzyn-

ski. The Araucaria Project: the Local Group Galaxy WLM–Distance and metallicity from quantitative spectroscopy of blue Supergiants. *ArXiv e-prints*, 805, May 2008.

S. van den Bergh. The outer fringes of the local group. *AJ*, 107:1328–1332, April 1994. doi: 10.1086/116946.

D. A. VandenBerg, P. A. Bergbusch, and P. D. Dowler. The Victoria-Regina Stellar Models: Evolutionary Tracks and Isochrones for a Wide Range in Mass and Metallicity that Allow for Empirically Constrained Amounts of Convective Core Overshooting. *ApJS*, 162:375–387, February 2006. doi: 10.1086/498451.

K. A. Venn, E. Tolstoy, A. Kaufer, E. D. Skillman, S. M. Clarkson, S. J. Smartt, D. J. Lennon, and R. P. Kudritzki. The Chemical Composition of Two Supergiants in the Dwarf Irregular Galaxy WLM. *AJ*, 126:1326–1345, September 2003. doi: 10.1086/377345.

K. A. Venn, M. Irwin, M. D. Shetrone, C. A. Tout, V. Hill, and E. Tolstoy. Stellar Chemical Signatures and Hierarchical Galaxy Formation. *AJ*, 128:1177–1195, September 2004. doi: 10.1086/422734.

A. B. Whiting, G. K. T. Hau, and M. Irwin. A New Local Group Galaxy in Cetus. *AJ*, 118:2767–2774, December 1999. doi: 10.1086/301142.

A. J. Youngblood and D. A. Hunter. The Luminosity Functions and Size Distributions of H II Regions in Irregular Galaxies. *ApJ*, 519:55–68, July 1999. doi: 10.1086/307366.

R. Zinn and M. J. West. The globular cluster system of the galaxy. III - Measurements of radial velocity and metallicity for 60 clusters and a compilation of metallicities for 121 clusters. *ApJS*, 55:45–66, May 1984. doi: 10.1086/190947.